Thermal-Driven Graupel Generation Process to Explain Dry-Season Convective Vigor over the Amazon

Authors: Toshi Matsui[1&2], Daniel Hernandez-Deckers[3], Scott E. Giangrande[4], Thiago S. Biscaro[5], Ann Fridlind[6], and Scott Braun[1]

[1] *Mesoscale Atmospheric Processes Laboratory, NASA Goddard Space Flight Center, Greenbelt, MD, USA*

[2] *Earth System Science Interdisciplinary Center – ESSIC, University of Maryland, College Park, MD, USA*

[3] *Grupo de Investigación en Ciencias Atmosféricas, Departamento de Geociencias, Universidad Nacional de Colombia, Bogotá, Colombia*

[4] *Environmental and Climate Sciences Department, Brookhaven National Laboratory, Upton, NY, USA*

[5] *Meteorological Satellites and Sensors Division, National Institute for Space Research, Cachoeira Paulista, São Paulo, Brazil*

[6] *NASA Goddard Institute for Space Studies, New York, NY, USA*

Submitted to EGU Atmospheric Chemistry and Physics (ACP)

Correspondence to: Toshi Matsui, Toshihisa.Matsui-1@nasa.gov

23 **Abstract**. Large-eddy simulations (LESs) are conducted for each day of the intensive observation

24 periods (IOPs) of the Green Ocean Amazon (GoAmazon) field campaign to characterize the

25 updrafts and microphysics within deep convective cores while contrasting those properties

26 between Amazon wet and dry seasons. Mean Doppler velocity (V_{dop}) simulated using LESs are

27 compared with 2-year measurements from a Radar Wind Profiler (RWP) as viewed by statistical

28 composites separated according to wet and dry season conditions. In the observed RWP and

29 simulated LES V_{dop} composites, we find more intense low-level updraft velocity, vigorous graupel

30 generation, and intense surface rain during the dry periods than the wet periods. To investigate

31 coupled updraft-microphysical processes further, single-day golden cases are selected from the

32 wet and dry periods to conduct detailed cumulus thermal tracking analysis. Tracking analysis

33 reveals that simulated dry-season environments generate more droplet-loaded low-level thermals

34 than wet-season environments. This tendency correlates with seasonal contrasts in buoyancy and

35 vertical moisture advection profiles in large-scale forcing. Employing a normalized time series of

36 mean thermal microphysics, the simulated cumulus thermals appear to be the primary generator of

37 cloud droplets. When subsequent thermals penetrate the ice crystal layer, droplets within the

38 thermals interact with entrained ice crystals, which enhances riming in the thermals. This appears

39 to be a production pathway of graupel/hail particles within simulated deep convective cores. In

40 addition, less-diluted dry-case thermals tend to be elevated higher, and graupel grows further

41 during sedimentation after spilling out from thermals. Therefore, greater concentrations of low-

42 level moist thermals likely result in more graupel/hail production and associated dry-season

43 convective vigor.

1. Introduction

Deep convection is a fundamental process of turbulence that drives the Earth's general circulation and regulates thermodynamic fields (Emanuel et al., 1994). Deep convection undergoes complex dynamical and microphysical processes throughout its life cycle, which appear as towering clouds visible from satellites in different parts of the world (Stephens et al., 2002). As a result, deep convection generates significant amounts of atmospheric latent heat, surface precipitation, and hydrometeors that reflect/absorb solar and infrared radiation, modifying atmospheric circulation and surface energy and mass fluxes (Hartmann, 2016). These complexities in deep convection and feedback processes pose significant challenges in predicting weather and climate using numerical Earth system modeling across different scales (Grabowski and Petch, 2009; Sullivan and Voigt, 2021).

57

Characteristics of deep convection are unique in different seasons and geographic regimes affected by the local environment. One of the most straightforward yet most robust regime separation concepts is the land-ocean (L-O) contrast (Williams and Stanfill 2002). Solar radiation increases the surface skin temperature over land more readily than over the ocean due to the smaller heat capacity of soils and vegetation than deep water bodies, thus producing stronger surface infrared flux and turbulent heat flux (Matsui and Mocko 2014). This greater surface energy deepens planetary boundary layers that may trigger deeper convective clouds depending on the atmospheric profiles (Pielke 2001). Overall, the continental environment tends to promote deeper convection with stronger, wider convective cores (Lucas et al. 1994, Wang et al. 2019), with suppressed warm rain and enhanced cold precipitation process (Williams et al. 2005), which often leads to unique drop-size distribution characteristics and precipitation partitioning between convective and stratiform process outcomes in different geographic regions (e.g., Tokay and Short 1996; Giangrande et al. 2012; Dolan et al. 2018).

71

Satellite observations similarly depict continental convective invigoration as characterized by more frequent lightning flashes and heavily rimed particles aloft over land than ocean (Williams et al. 2004, Zipser et al. 2006, Stolz et al. 2015, Matsui et al. 2016). Takahashi et al. (2017 & 2021)

75   show that continental convection generally contains less diluted cores than their oceanic

76   counterparts, following an inverse relationship between convective core width and dilution rate.

77   Similarly, Jeyaratnam et al. (2020) recently suggested that convective updraft and mass flux

78   properties were distinctly different between tropical land and tropical oceanic convection using

79   methods to estimate those properties that blend satellite observations with plume models. Hereafter,

80   we define "convective vigor" by the enhanced cold-precipitation process characterized by larger

81   rimed particles (graupel/hail) and large and copious raindrops in convective cores.

82

83   Representation of deep convective cloud land-ocean contrasts is still an ongoing challenge for

84   global atmospheric models at storm-resolving resolution (a few km of horizontal grid spacing),

85   partially owing to the poor representation of cloud dynamics (Matsui et al. 2016). Robinson et al.

86   (2011) configured idealized simulation setups to investigate the "island" effect of convection with

87   finer grid spacing (500 m or 1 km) and successfully simulated convective vigor equivalent to the

88   observed microwave brightness temperature. Matsui et al. (2020) used a nested regional model

89   with 1 km grid spacing to compare mid-latitude continental versus tropical maritime storms and

90   successfully reproduced land-ocean contrasts of hydrometeor identification profiles from

91   polarimetric radars.

92

93   However, statistical evaluation of simulated vertical velocity and association with convective

94   vigor process (i.e., graupel/hail generation) have not yet been examined very well due to a lack of

95   observations and detailed process-oriented model investigation, respectively. For example,

96   mesoscale convective system (MCS) studies performed by Prein et al. (2022) and Ramos-Valle et

97   al. (2023) highlight the challenges when attempting to represent continental convection within the

98   constraints of limited observations while attempting to establish optimal configurations as a

99   function of model grid spacing for typical midlatitude (Oklahoma) and tropical continental

100   (Amazon) conditions.

101

102   The 2-year measurements from the Green Ocean Amazon (GoAmazon) campaign provide

103   unprecedented data on the vertical velocity of deep convection by the Atmospheric Radiation

104   Measurement user facility (ARM, ARM Mobile Facility (AMF), Martin et al. 2017, Giangrande

105   et al. 2017). Recently, Giangrande et al. (2023) contrasted the thermodynamics and lifecycle

properties, including the vertical air velocity within isolated convective clouds observed during the Amazon wet and dry seasons, and found that dry-season convection exhibited more intense low-level updrafts and larger reflectivity associated with smaller convective cell areas than wet-season counterparts. Dry-season convection also tended to exhibit a shorter life cycle and often achieved maximum updraft and precipitation intensity at earlier life cycle stages than wet-season storms. Pre-convective thermodynamics profiles from those events revealed that the dry season showed a stronger deficit of dew-point temperature in the middle troposphere and higher values of mean-layer convective available potential energy (MLCAPE) at lower levels.

In addition to primary thermodynamic transitions between wet and dry season convective regimes (e.g., Giangrande et. al. 2020), the Amazon dry seasons may experience larger concentrations of aerosols due to biomass burning that have been recently associated with potential secondary contributions to changes in storm precipitation properties and convective vigor (e.g., Lin et al. 2006; Wang et al. 2018; Öktem et al. 2023). Moreover, the Amazon dry (wet) season has long been suggested to promote a continental (maritime) convection contrast for a given thermodynamic profile and background aerosols (Williams et al. 2002). Typical land-ocean contrast is characterized by a "hot" continental surface (Williams and Stanfill 2002) and sea-breeze type of mesoscale dynamics due to the thermal-patch effect (Robinson et al. 2011). Thus, instead of focusing on the complex nature of land-ocean contrast or other active versus break monsoonal contrasts performed globally (e.g., Holland et al. 1986, Keenan and Carbone 1992, Pope et al. 2009, Wu et al. 2009), the dry-wet season contrasts over the Amazon basin allows a unique emphasis on the impact of thermodynamic profiles and large-scale dynamics upon the formulation of convective vigor.

The main objective of this paper is to investigate dry-wet seasonal contrast and potential changes in the evolution of deep convection cloud processes using an LES model and forward simulations of Doppler radar observations. This attempts to reveal dynamical and microphysical processes that explain the observed dry-wet contrasts, focusing on the bulk controls imposed by the background thermodynamic profiles and large-scale forcing. The motivation for these efforts is the argument that an improved understanding of these dry-wet contrasts should facilitate untangling the more complex processes of land-ocean contrasts in deep convection. For this study, we employ a series

137   of daily large-eddy simulations (LESs) with bulk single-moment microphysics throughout the

138   GoAmazon campaign dry and wet season intensive observation periods (IOPs) to characterize dry-

139   wet season contrast in convection. These simulations are validated against the cumulative statistics

140   of ground-based Doppler velocity measurements during those periods. A thermal tracking analysis

141   is conducted to select golden cases from these dry- and wet-season LES runs to investigate the

142   physical process of convective vigor further. This effort focuses on thermodynamic impacts and

143   cloud dynamical roles in this manuscript, while the aerosol effects will be investigated in another

144   study.

145

146   Section 2 describes the general methodology and tools, including radar profilers, LES,

147   instrumental simulators, large-scale meteorological forcing, and thermal-tracking algorithms for

148   this study. Section 3 shows the results of the dry-wet contrast of meteorological forcing, statistical

149   composites of Doppler velocity, and thermal tracking analysis. Section 4 summarizes a thermal-

150   driven process of dry-season convective vigor, its uncertainties, and future directions.

151

152

153   **2.   Methods**

154

155   **2.1 GoAmazon: RWP Observations**

156

157   The primary datasets for this study are those collected by the 1290 MHz ARM Radar Wind Profiler

158   (RWP) operated during the U.S. Department of Energy's ARM ARM facility deployment during

159   its "Observations and Modeling of the Green Ocean Amazon 2014–2015" (GoAmazon) campaign

160   near Manaus, Brazil, from March 2014 through December 2015 (e.g., Martin et al., 2017). The

161   RWP was configured for precipitation sampling that included frequent vertical pointing to collect

162   conventional radar reflectivity factor Z and mean V_{dop} profiles through deep convective cells to

163   approximately 17 km in altitude (e.g., Giangrande et al. 2013, Giangrande et al. 2016, Wang et al.

164   2019, Williams et al. 2023). For measurements collected at these ultra-high frequencies and

165   without expectations for larger hail in Amazon deep convective storms (Liu and Zipser 2015, Bang

166   and Cecil 2019), all radar estimates are assumed as within Rayleigh scattering regimes, and

167   measurements are unattenuated in rain. The RWP deployed during GoAmazon had a beam width

168   of approximately 10 degrees thus horizontal measurement resolution is typically less than 1 km,

169   with a 200 m vertical (bin, gate) resolution and 10-s intervals between consecutive radar profiles.

170   All radar measurements were calibrated against a reference laser disdrometer collocated at the

171   main AMF site during the campaign (e.g., Wang et al. 2018), and a detailed method is discussed

172   in Williams et al. (2023).

173

174   For observation and simulation comparisons, the deep convective core is defined by using

175   thresholds applied to the observed and simulated RWP profiles: 1) column-maximum reflectivity

176   is greater than 35 dBZ, and 2) column-maximum V_{dop} is greater than 5 m/s. The choice for these

177   criteria is admittedly flexible, as model-vs-observed Z thresholds, in particular, are not necessarily

178   well-posed for convective-stratiform segregation such as removing all stratiform cells (e.g., Steiner

179   et al. 1995). Still, the additional velocity constraint afforded by the vertically-pointing RWP and

180   statistical representation of convective and stratiform composites seems to be reasonable (not

181   shown here), noting what is important is an attempt to apply thresholds for both observations and

182   simulations. A slightly different threshold does not alter the conclusions. Note that events on

183   3/19/14, 3/20/14, and 3/23/14, as well as the 10/4/14 cases from the dry season IOP, are clear

184   examples of Amazon mesoscale convective systems (MCSs, e.g., Wang et al. 2019). Thus, these

185   cases have also been removed from our statistical analysis to focus on isolated convective days.

186

187

188   **2.2 GoAmazon LES, Forcing, and Simulator**

189

190   GoAmazon LES runs utilize the Goddard Cumulus Ensemble (GCE), a cloud-process model

191   developed and improved at NASA GSFC over several decades (Tao *et al.* 2014). The GCE is

192   driven by large-scale forcing (LSF) with cyclic boundary conditions to generate cloud dynamics

193   and microphysics processes in Cartesian grid coordinates. No additional heat, moisture, or

194   momentum enters the domain apart from that imposed by the LSF or solar/infrared radiative

195   processes. In addition, GCE's anelastic dynamic core option allows faster integration of finer-

196   resolution runs (up to 1.5~2 times) than its compressible dynamic core option.

197

198   GoAmazon LES runs use 200-m horizontal grid spacing with 512 x 64 x 128 grids (x-y-z cartesian

199   coordinates) with a 2-second model time step. Vertical grid spacings stretch from near surface

200   level (starting from 44 m) and reach 200m around 4 km level, not to exceed horizontal resolution.

201   Thus, the domain covers a 102 km x 12.8 km area; this "narrow channel" domain setup intends to

202   resolve three-dimensional large eddies (i.e., thermals) while minimizing computational cost in

203   order to run LES for the entire IOPs. In terms of model physics, the 1.5-order turbulent kinetic

204   energy (TKE) scheme is used for subgrid turbulent mixing, and the Goddard radiation scheme is

205   used for computing radiative flux and heating (Chou and Suarez 1999 & 2001, Matsui et al. 2018).

206   The Goddard bulk one-moment 6-class scheme (4ICE hereafter) has four ice classes and uses

207   preset size and density mapping for snow, graupel, and hail (Lang et al. 2014; Tao et al. 2016).

208   4ICE successfully generated a realistic L-O contrast of convective-core hydrometeor distributions

209   compared to polarimetric radar retrievals in the previous study (Matsui et al. 2020). Also, note that

210   the one-moment scheme is unaffected by the background aerosol concentrations to focus on the

211   impact of thermodynamic and large-scale forcing on convective vigor in this study.

212

213   The LSF is derived from the VARiational ANALysis (VARANAL) approach, which is a broadly

214   accepted method for generating large-scale forcing wherein data are collected and adjusted based

215   on the vertical integration of the atmospheric mass, moisture, dry static energy, and momentum

216   budgets (Zhang and Lin 1997, Zhang et al. 2001, Xie et al. 2004). The VARANAL approach is

217   applied to the GoAmazon field campaign using ERA-Interim reanalysis (Dee et al., 2011) and

218   constrained by radar-based surface precipitation rate (Tang et al. 2016). The horizontal/vertical

219   advective forcings, mean wind profiles, and surface heat fluxes from the GoAmazon LSF are used

220   to drive the LES. These fields are interpolated and imposed as tendency terms at every model time

221   step. Our previous research demonstrated that GCE reproduced the observed precipitation quite

222   well when forced by the GoAmazon LSF (Tao et al. 2022). GoAmazon LESs are run from

223   September 2014 to 10 October 2014, defined as the dry-season IOP, and also run from 14 February

224   2014 to 26 March 2014, defined as wet-season IOP, as suggested by thermodynamic behaviors

225   characteristic of larger dry and wet-season expectations, respectively (Giangrande et al. 2017,

226   2020). Each daily LES is initialized at 12 AM local time from the LSF and integrated just for 30

227   hours rather than continuously integrated during the entire IOPs because the convection life cycle

228   typically follows a strong diurnal cycle due to the solar heating cycle, excepting propagating

229   organized convection (Tang et al. 2016, Giangrande et al. 2017, 2020). As a default setting, hourly

230   LES outputs are used to analyze the mean seasonal behavior of LESs.

231

232   Hourly LES outputs include an additional Doppler velocity field, corresponding to an expected

233   RWP observation through a multi-instrumental simulator, Goddard Satellite Data Simulator Unit

234   (G-SDSU, Matsui et al. 2014a; Matsui et al. 2014b). In this study, a ground-based Doppler radar

235   simulator is implemented in the model to replicate RWP observable signals. Radar backscatter is

236   estimated from nonRayleigh calculations with a Maxwell-Garnett assumption of air-water-ice

237   mixtures at 1290 MHz frequency, though for the RWP frequency, vertical pointing, and media

238   type/size expectations therein, the forward modeling is more straightforward than most weather

239   radar wavelength applications and appropriate for Rayleigh scattering assumptions. Doppler

240   velocity is estimated using pressure-adjusted hydrometeor terminal velocities weighted by radar

241   backscatter spectrum for each particle size distribution (PSDs). All these single scattering

242   calculations follow the 4ICE microphysics calculation/assumptions of particle size, density, and

243   phase for each hydrometeor species for physics consistency (Matsui et al. 2014b). Finally,

244   simulated signals are averaged consistent with the RWP beamwidth (10 degrees). This beamwidth

245   implies different averaging at different heights, for example, corresponding to six horizontal grids

246   of the LESs being averaged for a representative output at the 15 km height. Overall, this beamwidth

247   averaging smear LES-scale Doppler velocity signal statistics closer to the anticipated observed

248   instrumental signals (Matsui et al. 2014b). However, it should be noted that the exact sampling

249   methods are different between observations and simulations. For example, the RWP observations

250   are vertical pointing measurements that collect profiles at 6-second ("instantaneous") intervals. In

251   contrast, the modeled RWP signals are drawn from a domain-wide sampling of hourly LES outputs.

252

253

254   **2.3 Thermal Tracking Algorithm**

255

256   The thermal tracking method used here is described in detail by Hernandez-Deckers and Sherwood

257   (2016), who improved the initial version used by Sherwood et al. (2013). It is an offline algorithm

258   that uses high temporal resolution output (~1 min) from LES to identify and track coherent rising

259   volumes of cloudy air, i.e., thermals. The algorithm first identifies all peak vertical velocities larger

260   than 0.8 m/s that have water condensate content of at least 0.01 g/kg at every available snapshot

261   of the simulation and matches peaks from successive snapshots to identify the available points of

262   the trajectories of rising cloudy air parcels. A third-order polynomial is fitted to these points to

263   reconstruct smooth trajectories and to allow a precise estimate of the ascent rate of the rising air

264   volume at each snapshot. Notice that this ascent rate differs from the actual vertical velocity at a

265   particular grid point since thermals develop internal toroidal circulations such that the peak vertical

266   velocity at their centers is higher than the actual ascent rate of the air volume (e.g., Blyth et al.

267   2005; Sherwood et al. 2013).

268

269   The extent of each rising air volume (the size of each thermal) is estimated assuming a spherical

270   shape centered at its smoothed trajectory, ensuring that the average vertical velocity of the enclosed

271   volume matches that obtained from the derivative of the trajectory. Tracked thermals must fulfill

272   certain requirements; for example, they must be tracked for at least three time steps, their radius

273   must be larger than twice the horizontal grid spacing, their time-average ascent rate must be at

274   least 1 m/s, their change in size in between successive snapshots must be less than 80% of the

275   smallest radius, and most importantly, their trajectories must be consistent with their vertical

276   momentum budget. The momentum budget of a tracked thermal is computed from its buoyancy

277   (obtained from the density field), the pressure gradient force (obtained by integrating the pressure

278   field over the entire thermal's surface), a "resolved mixing term" (obtained from the convergence

279   of vertical momentum flux across the thermal's surface), and an entrainment or detrainment

280   contribution due to the change in size between snapshots. This allows us to compute the expected

281   final position of each thermal based only on its initial ascent rate, which is compared with the

282   thermal's last tracked position. The distance between the actual and expected final positions must

283   be smaller than the average thermal diameter and smaller than 20 % of the vertical distance

284   traveled; otherwise, the thermal is discarded.

285

286   Once thermals are tracked with this algorithm, many properties can be studied based on all

287   available model variables of interest. For example, average values for each thermal, such as ascent

288   rate, size, altitude, entrainment rate, etc., are easily computed. Also, composites of different

289   quantities can be obtained for different "stages" of a thermal's lifecycle. Typically, thermals exhibit

290   one maximum ascent rate throughout their lifetime, which indicates their most vigorous phase.

291   This time step is used as a time reference common (t=0) to all thermals to create composites of

292   various properties at different stages of thermal lifetimes. Note that our tracking algorithm cannot

293   analyze merging or splitting thermals, regardless of their occurrence. This limitation requires

294   further study.

295

296   This thermal tracking algorithm was first used to study the main properties of cumulus thermals in

297   simulations of transient-growing convection (Sherwood et al., 2013; Hernandez-Deckers and

298   Sherwood, 2016) and provided strong evidence that thermals are typically small, short-lived (4-5

299   minutes on average), and mix vigorously with their environment. Also, Hernandez-Deckers and

300   Sherwood (2016) showed that the spherical shape approximation is generally valid and that

301   thermals, rather than plumes, are a more realistic building block for cumulus clouds. Hernandez-

302   Deckers and Sherwood (2018) used this algorithm to study the mixing properties of thermals in

303   more detail and contrast them with known parameterizations. Results from these studies have set

304   up the stage for a deeper understanding of cumulus dynamics and for further studies that use

305   different approaches (e.g., Gu et al., 2020; Morrison et al., 2020; Peters et al., 2020; Xu et al.,

306   2021; Morrison et al., 2023). Recently Hernandez-Deckers et al. (2022) used this algorithm to

307   study aerosol-deep convection interactions, highlighting the importance of the strong coupling

308   between microphysics and small-scale dynamics in convective clouds. Here we run this tracking

309   algorithm with the GCE model output for 5 hours starting at 1900Z (3 pm local time) on 09/07/14

310   (dry case) and 02/26/14 (wet case), using 1-minute interval output.

311

312

313   **3. Results**

314

315   **3.1 Dry-Wet Contrast of Large-Scale Forcing**

316   Campaign atmospheric thermodynamic profiles and the typical variability observed during

317   GoAmazon dry and wet seasons have been previously depicted using composite radiosonde skew-

318   T log-P diagrams (e.g., Giangrande et al., 2017, 2020, 2023). These depictions often show very

319   similar temperature profiles between dry and wet seasons, whereas the moisture profiles indicate

320   apparent differences, highlighting the mid-level deficit of the dew-point temperature profile in dry-

321   season composites. Since this study utilizes LSF to drive LESs, seasonal thermodynamics and

322   dynamics are re-characterized by the LSF (Tang et al. 2016).

323

324   In Fig. 1, we plot a time series of apparent moisture sinks (Q2), vertical moisture advection, and

325   parcel potential buoyancy profiles with surface precipitation rate from GoAmazon LSF for the

326   IOPs. These time series of LSF profiles are integrated and contrasted in terms of Contoured

327   Frequency by Altitude Diagrams (CFADs, Yuter and Houze 1995) as the dry and wet season IOPs

328   (Figure 2).

329

330   Here, Q2 is the sum of changes in moisture content, horizontal moisture advection, and vertical

331   moisture advection (Yanai et al. 1973), balanced with net condensation rate and turbulent transport

332   of moisture vertical advection. Large Q2 corresponds to a large atmospheric moisture loss due to

333   net condensation loss (i.e., precipitation). Large Q2 is associated with intervals with heavier or

334   more widespread surface precipitation; thus, dry-IOP Q2 and surface precipitation are typically

335   smaller than wet IOP (Fig. 1a-b). Similarly, Figs. 1c-d shows that peaks of vertical moisture

336   advection term coincide with those peaks in the Q2 rate. Note that the Q2 rate in tropical

337   environments is mainly contributed by the vertical moisture advection term rather than the

338   horizontal advection term (not shown here). More importantly, positive (red shade) vertical

339   moisture advection of the wet IOP tends to be stretched up to higher altitude (up to 200 mb) than

340   the dry IOP (up to 600 mb) in most cases.

341

342   As previously discussed by Tang et al. (2016), the associated Amazon Q2 CFADs show the largest

343   positive Q2 between 700 and 400 mb, while the largest negative Q2 is around 800 mb (Figs. 2a-

344   b). The Dry-wet composite CFAD highlights more frequent positive Q2 values above the 800 mb

345   level during the wet IOP. In contrast, more frequent negative Q2 during the dry IOP (Fig. 2c).

346   Vertical moisture advection depicts similar CFAD shapes (Figs. 2d-e). Still, it highlights high

347   frequencies of low-level positive vertical moisture advection and mid-to-low-level negative

348   moisture vertical advection in the dry IOP in comparison with the wet IOP.

349

350   Finally, in Figs. 1e-f we plot the time series of parcel potential buoyancy profiles (positive

351   components only), computed from LSFs by lifting surface airmass dry and moist adiabatically.

352   These potential buoyancy magnitudes are not necessarily associated with precipitation intensity.

353   Potential buoyancy CFADs show peak forcing between the 600 mb and 200 mb levels (Figs. 2g,

354   h, & i). The wet IOP suggests a larger variability of potential buoyancy at the upper troposphere

355   than the dry IOP (Figs. 2g-h). Potential buoyancy appears to be slightly stronger in the dry IOP,

356   and concentrated in a relatively lower troposphere than its wet IOP counterpart (Fig. 2i), which

357   agrees with findings in Giangrande et al. (2023). These results will be further discussed along the

358   thermal concentrations in the latter section.

359

360

361   **3.2 Dry-Wet Composite of Doppler Velocity CFADs**

362

363   Giangrande et al. (2023) highlighted dry-wet seasonal characteristics of storm vertical air motions

364   retrieved using RWP. They found that daytime isolated dry season convective cells tend to have

365   stronger updrafts at altitudes below the melting level. Yet, unlike their wet-season counterparts,

366   updrafts do not increase in intensity much above the melting layer. However, dry-season

367   convective cores were also characterized by stronger downdrafts at all altitudes, especially when

368   compared to wet-season counterparts aloft. Our present study utilizes similar direct measurements

369   of the mean V_{dop} from RWP to characterize the dry-wet contrast of deep convective cores. The

370   advantage of using V_{dop} measurements is that the quantity is the direct radar measurement and

371   helps reduce uncertainties from retrieval assumptions, such as requiring hydrometeor

372   identification or associated terminal fall speed corrections if the intent was to retrieve the vertical

373   air motion (Giangrande et al. 2013, 2016). Here, vertically-pointing V_{dop} measurements contain

374   sufficient information to evaluate storm characteristics, with the understanding that these

375   measurements represent the terminal velocities of hydrometeors combined with the vertical air

376   motion.

377

378   In Fig. 3a, we provide the cumulative sample numbers of CFADs (for each bin of V_{dop} and altitude)

379   as simulated and subsampled from the LES hourly outputs from the combined dry and wet season

380   IOPs. If the sampling numbers are normalized for each altitude, the Vdop CFADs will be formed.

381   Fig. 3b shows the sum of hydrometeor mass concentrations from each V_{dop}-altitude bin. Namely,

382   each hydrometeor mass concentrations from "cloud", "rain", "graupel-plus-hail", or "ice-plus-

383   snow" are separately accumulated for each bin. The larger number of samples associated with a

384   larger accumulated mass concentration of hydrometeor can generate the "representativeness" of

385   the hydrometeor class for a given V_{dop}-altitude bin location. Because V_{dop} is the sum of the vertical

386   velocity of the air and the terminal velocity of hydrometeor particles weighted by their reflectivity,

387   this plot facilitates understanding V_{dop} CFAD.

388

389   As mentioned above, we defined four regimes based on the accumulated mass of each hydrometeor

390   category. The "cloud" category (CL) is centered around -5 m/s of V_{dop} and 4 km altitude, slightly

391   overlapping with other categories. A "rain" category (RA) is more narrowly concentrated around

392   -8 m/s of V_{dop} and below 4 km altitude. The "graupel-plus-hail" category (GH) is centered around

393   -14 m/s of V_{dop} at 5 km altitude. Finally, an "ice-plus-snow" category (IS) is narrowly concentrated

394   along -1 m/s of V_{dop} above 5 km altitude. These locations roughly correspond to each hydrometeor

395   category's altitude and terminal velocity when factoring in the background/ambient vertical air

396   velocity. Note that our "cloud" regime has no terminal velocity in GCE 4ICE microphysics, thus

397   V_{dop} represents or tracks the background vertical air velocity and overlaps with the other regimes.

398   Moreover, simulated V_{dop} and hydrometeor statistics are also sensitive to model physics and those

399   assumptions to some degree. For example, any real-world cloud regime may be extended to higher

400   altitudes, but the model 4ICE microphysics scheme tends to quickly convert cloud liquid to cloud

401   ice category due to saturation adjustment (See Figs. 14-16 of Matsui et al. 2023). Nevertheless,

402   this representative mapping will help discuss the variability of the V_{dop} CFADs between the dry

403   and wet season IOPs.

404

405   In Fig. 4, we provide an observed and simulated climatology of V_{dop} CFADs as sampled from deep

406   convective cores and summarized over the dry and wet season IOPs. In both the dry and wet season

407   IOPs, the observed CFADs depict a smoother transition of the V_{dop} at the freezing level into the

408   melting layer (4-5 km, Figs. 4a-b). At the same time, simulations show a more abrupt transition

409   around the freezing layer (Figs. 4d-e). This is primarily because bulk single-moment microphysics

410   more abruptly converts solid to liquid phases through autoconversion than explicit bin-resolving

411   microphysics (Iguchi et al. 2014). This rapid conversion also overestimates the terminal velocity

412   of raindrops near and just below the freezing level. Another possible reason is overestimating the

413   graupel/hail size, leading to larger melted raindrops with high terminal velocity.

414

The CFADs have been summarized according to dry and wet season IOPs to explore these seasonal contrasts between the deep convective cores (Figs. 4c, 4f). In the R regime (green box), the dry IOP suggests more prevalent samples in strongly negative V_{dop} for our observations and simulations, indicating that deep convective cores during the dry season IOP tend to have more vigorous, faster-falling (larger) raindrops. In the GH regime (purple box), the dry season IOP dominates the sampling. The observations indicate this dominance (red shade) up to 10 km altitude (the extent that observations were included), while the simulation shows this behavior up to 8 km, suggesting LES underestimation in graupel/hail altitudes. In the CL regime, the observations and the simulations agree well, except that some sampling is overwhelmed by the dry season IOP behaviors in the overlapped area. This likely indicates a shift in the presence of stronger low-level updraft velocities, consistent with the analysis in Giangrande et al. (2023).

When considering the IS regime, there are examples of agreements and discrepancies between the observations and simulations. One key agreement is that the wet IOP dominates the samples in the area of positive V_{dop} above 8 km altitude. This indicates that observations and simulations suggest a shift towards stronger upper-level vertical air velocity for the wet season IOP examples than for the dry season IOP. This is consistent with the absence of dry mid-levels and the stochastic updraft model expectations from Giangrande et al. (2023). On the other hand, the observations indicate a more dominant sampling of velocities during the wet season IOP at around -3 m/s of V_{dop}, whereas simulations change the dominant sampling mode from wet to dry IOPs at around 7 km altitude. This is a potential bias in single-moment bulk microphysics, which tends to glaciate cloud droplets or raindrops more quickly into ice particles than double-moment schemes (e.g., Fig. 16 of Matsui et al. 2023). The observed composite also shows more dry-season dominant frequencies in GH zones than the simulation, indicating the underestimation (overestimation) of raindrop/graupel (ice/aggregate) particles above 7 km height.

Excepting this discrepancy in the IS regime, dry-wet composites of V_{dop} CFAD agree well between observations and simulations, suggesting that LES could successfully represent the important nature of dry-wet contrast, i.e., dry-season convection tends to generate stronger low-level updraft

444 velocity, generating more graupel/hail, and vigorous raindrops accompanied with stronger low-
445 level downdraft than the wet season.

446

447 To further investigate these seasonal shifts in core properties, golden cases are selected to analyze
448 deep convection lifecycle and processes. Golden cases are two single-day simulation cases, one
449 for dry and one for wet season, representing V_{dop} CFADs of each season. For this, the V_{dop} CFADs
450 are constructed for each day during the wet and dry season IOPs, and these daily CFADs are
451 compared to the composites of seasonal CFADs (not shown here). After day-to-day analysis of
452 correlation and root-mean-square errors between daily and seasonal CFADs, the convective event
453 on the 2/26/14 case is selected to represent the wet IOP convections. In contrast, the 9/7/14 case is
454 chosen to represent dry IOP convection. Fig. 5 shows a dry-wet composite of V_{dop} CFAD using
455 these two case studies. This figure compares quite well with the seasonal composite of V_{dop} CFAD,
456 having the dry convective vigor signals and model biases of the seasonal composite (Fig. 4f).

457

458 In Fig. 6, we show a time series of domain-mean profiles of convective cores drawn from these
459 dry- and wet-season golden cases, highlighting from 1600Z (1200 local time) of the starting day
460 to 0400Z (0000 local time) of the next day. The dry season golden event shows a clear diurnal
461 convection cycle, peaking at 2100-2200Z (local 5-6 pm). In contrast, the wet season golden event
462 shows an already ongoing, continuous sequence of deep convection with several embedded strong
463 pulses. Convective top heights reach up to 17 km for both the dry and wet events (Figs. 6a-b).
464 Low-level positive upward vertical velocity is more ubiquitous in the dry case, while upward
465 vertical velocity of the wet case extends to the middle-to-upper troposphere up to 15km (Figs. 6c-
466 d).

467

468 Dry-case graupel-plus-hail (GH) mass concentrations peak around 2100-2300Z when the
469 convective clouds reach their deepest cloud top heights, and the maximum GH concentration
470 exceeds that of the wet case. Rain mass concentrations peak between 2200Z and 00:30Z on the
471 subsequent day for the dry case, and this appears to be slightly more intense than the rainfall
472 simulated for the wet cases. Note that precipitation areal fraction is expected to be larger for the
473 wet season (i.e., Giangrande et al. 2016, 2023), such that dry-season convection is often
474 characterized by narrow yet intense isolated convection, while wet-season convection is

475 characterized by widespread moderate to deep convection (although with higher domain mass
476 flux). The intense surface rainfall rates are generally correlated with the generation of graupel,
477 frozen drops, and/or small hail particles during the dry-season convection, but there are some time
478 lags from 21Z to 22:50Z in the dry-case convection. This is because the initial convective core is
479 much narrower, and near-surface relative humidity is slightly low (~80%) around 21Z, and later
480 convective area increases so as near-surface relative humidity (~96%) around 21:50Z. Thus, more
481 surface rain evaporation likely suppresses surface precipitation during earlier convective periods.
482 These time series behaviors are generally consistent with the observed characteristics in the time-
483 integrated V_{dop} CFADs (Fig. 5).

484

485 One key question is why larger or heavily rimed particles tend to be preferentially generated in
486 dry-season convection compared to wet-season convection, given that both seasons indicate
487 convection with intense updraft velocity. This question follows previous efforts of Williams and
488 Stanfill (2002) for simulations of deep convection that contrasted land and oceanic clouds. For
489 example, while land and ocean environments may have similar convective available potential
490 energy (CAPE), differences in detailed potential buoyancy and vertical velocity profiles enable
491 additional graupel/hail particles to form in continental deep convection when compared to the
492 maritime environments (Matsui et al. 2020). A Lagrangian tracking analysis is performed to
493 examine this question for Amazon dry and wet season contrasts to investigate the dynamics and
494 microphysics within cumulus thermals for these dry and wet golden events (Section 3.3).

495

496

497 **3.3 Thermal Tracking Analysis**

498

499 Thermal tracking analysis (Section 2.3) was conducted over 5-hour periods from 1900Z to 0000Z
500 for the dry and wet season events using 1-minute LES outputs. Fig. 7 depicts normalized x-z cross-
501 sections of thermal properties at the moment of maximum vertical velocity in the dry and wet cases
502 and dry-wet differences. Thermals typically experience development and decaying stages in their
503 lifetime. During development, moist thermals increase their vertical velocity and size by releasing
504 latent heat and entraining surrounding air (Morrison et al. 2021). After defining and tracking each
505 thermal from the LESs, our normalizing procedure first defines the reference time from each

506   thermal's lifetime based upon peak vertical air velocity (denoted as thermal maxima) and then

507   conducts a weighting average of each thermal property at the thermal maxima only. Our weights

508   are based on the magnitude of thermal mass flux to avoid under-representing properties of less-

509   populated but vigorous thermals. Because these heights at thermal reference time are different for

510   each thermal in dry and wet case studies, averaging properties are somewhat biased toward thermal

511   vertical distributions (discussed later).

512

513   For example, in Fig. 7a we plot the weighted-average peak vertical air velocity (W) for the dry-

514   case thermal (9.6 m/s) and the wet-case thermal (10.6 m/s). Perhaps surprisingly, the flux- and

515   radius-weighted average dry-case thermal is slightly slower in W than that found for the average

516   wet-case. Here, we find that the vertical air velocity of the wet-case thermal is more

517   homogeneously distributed than its counterpart for the dry-case thermal, leading to higher

518   weighted-mean W despite weaker values at thermal centers (red shade in Dry-Wet plot, Fig. 7a).

519   Also, unexpectedly, supersaturation and cloud droplet mixing ratio (Qc) of the dry-case thermal

520   are elevated compared to the wet-case thermal (Fig. 6b-c), since wet-case thermals may be

521   expected to instead have higher supersaturation and/or more condensation owing to the higher

522   availability of water vapor (e.g., Giangrande et al. 2023).

523

524   Exploring the other classes, the rain mixing ratio (Qr) is similar between the dry-case and wet-case

525   thermals (0.17 g/kg), but graupel-hail concentrations (Qg+h) are significantly larger in the dry-

526   case thermals (0.95 g/kg) compared to the wet-case thermals (0.79 g/kg); this latter result is

527   consistent with previous discussions from event time-series in Fig. 6e. Cloud ice and snow mixing

528   ratio (Qi+s) values are slightly larger in the wet-case thermal (3.5 g/kg) than in the dry-case thermal

529   (3.2 g/kg). While this difference is not significant, this is also potentially a surprising outcome

530   since dry-case deep convective clouds might otherwise be expected to be deeper/stronger and thus

531   characterized by additional ice hydrometeor concentrations. However, some absence of these

532   media may be partially explained by following Giangrande et al. (2020; 2023) suggestions that

533   drier mid-to-upper levels in the dry season may limit periphery precipitation aloft (i.e., enhanced

534   evaporation). Overall, Qr and Qg+h seem to be concentrated in these composite averages

535   downward from the thermal core due to the gravitational sedimentation process. Supersaturation

536   and Qc, however, are also more vertically elongated than thermal properties established by

537 Hernandez-Deckers et al. (2022) using the Weather Research and Forecasting (WRF) model for a

538 case of scattered convection over Houston, Texas. Q_{i+s} is more homogeneously distributed across

539 the defined borders of thermals. Also, dry-wet differences show slight asymmetric results,

540 particularly in W, Q_r, and Q_{g+h}. These could be attributable to differences in horizontal wind

541 shear, evidenced by a greater tilt in the thermal centerline flow in the dry case (gray streamlines),

542 leading to greater concentrations in the tilt direction of more rapidly sedimenting quantities that

543 are formed within thermals (i.e., Q_r and Q_{g+h}); since thermal composites are not aligned with the

544 mean wind, such preferential outflow may not be fully captured by this analysis (i.e., asymmetric

545 signatures could be greater or lesser along other directions than X alignment).

546

547 An initial leading question is why the dry-case thermals have greater cloud water and

548 supersaturation on average. To further untangle these results in Fig. 7b-c, we derive the vertical

549 profiles of flux-weighted mean thermal states, now including all thermal times (Fig. 8a-g).

550 Immediately, these plots reveal striking differences between the thermal number concentration

551 (N) profiles for dry-case and wet-case examples (Fig. 8a; the number of thermals per km height

552 within the 102 km x 12.8 km domain). For instance, dry-case convection shows a larger

553 concentration of thermals below the 8 km height, while wet-case convection promotes a more

554 homogeneous thermal concentration that extends across most heights. This behavior is somewhat

555 reminiscent of the distribution for the difference in vertical moisture advection and potential

556 buoyancy profiles between the parent dry and wet season conditions (e.g., Fig. 1 and 2, discussions

557 in Section 3.1). Moreover, thermal generation in our LES responds to these terms partially from

558 the seasonal large-scale forcing.

559

560 According to the classic similarity theory of Morton et al. (1956), the width of dry/moist thermals

561 should increase with increases in the boundary layer depth (William and Stanhill 2002). For the

562 Amazon basin, previous GoAmazon studies such as Giangrande et al. (2017, 2023) showed that

563 dry season boundary layer height is generally deeper than that of the wet season, potentially on the

564 order of 200 m deeper for isolated deep convective events they tracked. Following this logic, dry-

565 case convection may anticipate larger thermals. However, LES thermal tracking analysis suggests

566 that the sizes (R) of thermals upon initiation appear to be quite similar between the wet and dry

567 events and then appear to grow at similar rates for several km before the dry-case thermal size

568   catches up with the moist size around 6 km in height, only to be overtaken again by the deeper

569   wet-case thermals around 9 km (Fig. 7b). Further, Fig. 8c shows the mean vertical velocity of

570   thermals, showing nearly identical updraft velocity below 4 km. However mean updraft velocity

571   profiles above 4 km are quite different between the dry and wet cases; e.g., the dry case peaks

572   around 8 km, while the wet case peaks at 6 and 10 km. This result implies that differences in moist

573   convection between dry and wet cases are poorly characterized by thermal sizes.

574

575   Qc in thermals also shows very similar profiles between the dry and wet cases (Fig. 8d). However,

576   because thermal numbers of the dry case are more concentrated at the lower troposphere (Fig. 8a),

577   all-height mean properties of dry-case thermals are characterized by more Qc (Fig. 7c). Qr of the

578   wet case is nearly twice as large as the dry case (Fig. 8e); however, normalized x-z cross-section

579   (Fig. 7d) does not show such a large difference (explained below). $Qi+s$ also shows similar

580   distributions (Fig. 8f). Still, total x-z mean $Qi+s$ is larger in the wet case than the dry case due to

581   larger thermal numbers in the upper troposphere (Fig. 7e). Uniqueness appears in thermal $Qg+h$

582   (Fig. 8g). While both dry and wet cases show similar magnitude of the peak values (~0.9 g/kg),

583   the peak height in the dry case is approximately 3 km higher than the wet case. This $Qg+h$ peak of

584   the dry case coincides with the peak of vertical velocity (Fig. 8c).

585

586   Fig. 8h-k displays these hydrometeor mixing ratios averaged over the same periods, including all

587   convective grids defined by vertical velocity greater than 1 m/s. Vertical profiles and dry-wet

588   differences are similar to the results in Fig. 6. However, compared with the in-thermal profile

589   results (Fig. 8d-g), it facilitates understanding of the convective core microphysics process. First,

590   mean in-thermal convective-grid hydrometeor concentrations are smaller than in-thermal profiles;

591   particularly in-thermal Qc values are roughly six times larger than convective-grid average Qc

592   (Figs. 8d & 8h), suggesting that thermals are major cloud droplet generators (Hernandez-Deckers

593   et al. 2022).

594

595   The convective-grid $Qg+h$ of the dry case is nearly twice as high as that in the wet case, peaked

596   around the melting layer (Figs. 8g & 8k), whereas in-thermal $Qg+h$ shows similar peak values

597   between the dry and wet cases. As indicated by Fig. 7g, these larger and heavier rimed particles

598   sediment from thermals and further collision with supercooled liquid must enhance the graupel

599 growth during the sedimentation process, as suggested from aircraft measurements (Blyth and
600 Latham 1993). Thus, elevated in-thermal Qg+h in dry-case convection can have further riming
601 growth after falling out from thermals. This vigorous growth of Qg+h in dry-case convection
602 eventually generates vigorous raindrops after the melting process. This could explain why
603 convective-grid Qr in the dry case is larger than that in the wet case (Fig. 8i), opposite from the
604 result of in-thermal Qr (Fig. 8e). Thus, in-thermal Qr values are not directly related to total Qr in
605 the convective core (or surface precipitation rate) because of this cold precipitation microphysics
606 process in deep convection.

607

608 A second leading question is why the height at the peak value of dry-case in-thermal Qg+h is more
609 elevated than the wet-case thermal (Fig. 8g). Fig. 9 shows histograms of thermal properties from
610 the dry and wet cases. Consistent with the mean vertical profiles (Fig. 8a), more thermals are
611 initiated below 7 km in the dry case than in the wet case (Z0, Fig. 9d). Thermal radius in the wet
612 case is also larger than the dry case regardless of shallower boundary layer depths in the wet case
613 (Fig. 9a), consistent with R in thermal vertical profiles reaching larger sizes at most elevations in
614 the wet case (Fig. 8b). However, here we see that thermal vertical velocity (W, Fig. 9b), travel
615 distance (dZ, Fig. 9c), and lifetime (Fig. 9e) in the dry case are all greater than in the wet case.
616 Thermal entrainment rate is smaller in the dry case than the wet case. These results indicate that
617 the thermals in the dry-case deep convection can travel longer distances with an extended lifetime
618 due to a lesser dilution.

619

620 Interestingly, slightly smaller thermal radii in dry-case convection can have a lower entrainment
621 rate than in wet-case convection. Hernandez-Deckers and Sherwood (2018) also found that the
622 variability of thermal radius can only account for 20% of the total variance of thermal dilution rate,
623 i.e., larger thermal tends to have a lesser dilution rate. This was concluded through similar thermal
624 tracking analysis from different LESs. Therefore, thermal size is not the sole parameter for
625 determining dilution rate.

626

627 Giangrande et al. (2022) suggest that the convective area is smaller in dry-season convection over
628 this region. Thus, this indicates that stronger low-level buoyancy in dry-season environments can
629 more narrowly concentrate updraft and low-level thermals in the area, thus creating less diluted

630   environments probably due to the impact of thermal drag (Romps and Charn 2015). This is merely

631   speculative and requires further investigation to confirm or refute. Takahashi et al. (2022)

632   investigated cloud-scale entrainment between continental and maritime environments and found a

633   larger dilution rate in maritime convection than in continental convection. Our results suggest that

634   this difference in cloud dilution happens from the thermal-process level. These conditions elevate

635   dry-case thermals and graupel peak concentration toward higher altitudes than the wet-case

636   convection (Fig. 7f), leading to greater graupel production.

637

638   Finally, time series of thermal properties in the x-z cross-section are constructed for the dry case.

639   For this, each thermal at its maximum w value is centered and defined as the time of zero, and

640   prior (later) steps are represented in negative (positive) time steps. Because of the 1-minute LES

641   output, the time series from -3 to 3 encompasses 7 minutes of time steps. This averaging process

642   also weighs upon the magnitude of the thermal mass flux (Hernandez-Deckers et al. 2022); thus,

643   thermals at larger values in positive and negative time steps tend to have a fewer sampling numbers.

644   Also, to make the composites, equal-sized thermals are sampled to characterize the mean time

645   series of thermal properties, avoiding sampling too small thermals, which often has no

646   supersaturation (Hernandez-Deckers and Sherwood. 2016). This normalization procedure ends up

647   with the result that maximum W values do not appear at reference time (t=0), but better capture

648   the evolution of the largest flux-bearing thermals (Fig. 10). We also note that a typical thermal

649   travel distance is 1.3 km (Fig. 9c) and a minority of dry-case thermals therefore contain either no

650   ice phase (Fig. 8e-f) or no liquid phase (Fig. 8c-d), but most contain both phases between 3 and 7

651   km. Note that this flux-weighting is the one way to present the results, while simple non-weighting

652   averaging can also show similar results.

653

654   In the dry case (Fig. 10), within thermals that experience an extended peak in W (6–11 m s^{-1}), the

655   average supersaturation, cloud, and rain mixing ratio peaks at the earlier steps and decreases

656   toward the end of the time steps. This indicates that a chunk of condensation heating is the main

657   initial driver of moist thermal growth. These thermal properties are typically centered around the

658   thermal core. By contrast, Qi+s properties are more homogeneous and less concentrated at the core

659   of thermals, and they tend to increase toward the end of the time series. Especially, the early stages

660   (t=-3, -2, & -1) indicate thermals are approaching an existing ice layer rather than generating ice

661   around the thermal core. In the later stages (t=1, 2, & 3), the Qi+s is weakly concentrated toward

662   the upper thermal cores. This evolution of Qi+s suggests that thermals are not the main initiator of

663   Qi+s at the beginning, while Qi+s is rather entrained into the thermal within the early stages of the

664   mixed-phase zone, at least using the single-moment bulk microphysics. On the other hand, after

665   liquid saturation is no longer contributing substantially to Qc, Qi+s becomes a leading destination

666   of the overall transfer from vapor to hydrometeor phases within thermals that remain vigorous,

667   probably due to the Bergeron process (Bergeron 1935). Further research is needed to investigate

668   the ice nucleation and growth process in greater detail throughout the different stages of thermals'

669   lifecycle.

670

671   On the other hand, Qg+h increases toward the peak time of thermals (t=0), and starts decreasing

672   toward the later time steps (t=3). The spatial concentration of Qg+h is also peaked around the

673   thermal cores, similar to W, rh, Qc, and Qr. The increase of Qg+h coincided with the timing of

674   thermal entrapment of Qi+s and a reduction in Qc and Qr for time steps between -3 and 0. This

675   suggests that large concentrations of in-thermal Qc and Qr collide with entrained Qi+s to enhance

676   the riming process, generating graupel and hail particles at the thermal core. Note that the 4ICE

677   scheme only allows wet growth (collecting supercooled liquid) of graupel, while dry growth

678   (collecting ice and aggregate) of graupel has been suppressed due to unrealistic graupel in

679   convective anvil (Lang et al. 2014). After the reference time step (t=0), Qg+h decreases, most

680   likely due to sedimentation exceeding production. As indicated by Fig. 8g & 8k, this spilled

681   graupel and hail can further grow by colliding with supercooled liquid particles until melting.

682   Taken together, this analysis also suggests that this vigorous Qg+h-generation process in the

683   convective core *does not* occur through the classic parcel-driven convection. Instead, these graupel

684   and hail generations are most likely driven by sequential interactions of thermal ensembles and

685   microphysical processes. Note that the time series of the wet case also shows a similar finding but

686   is biased toward the thermals in the upper atmosphere (not shown here).

687

688   In addition to reference time, we composited thermal properties at different altitude levels (Fig.

689   11). The method for sampling and compositing is the same as in Fig. 10. However, it characterizes

690   vertical profiles of thermal composites using altitude references from 2.5km up to 10.5km,

691   including the mean air temperature. Despite of different reference methods, altitude-reference plots

692 appear to be similar patterns to time-reference plots. Vertical velocity (W) increases toward the
693 peak level at 8.5 km, similar to the mean profile in Fig. 8c. There is strong supersaturation (S)
694 between 4.5 km and 6.5 km, which rapidly decreases above 8.5 km. Qc, Qr, Qi+s, and Qg+h
695 profiles also resemble thermal-mean profiles in Figs. 8d, 8e, 8f, and 8g, respectively. In thermal
696 cores, Qc, Qr, and Qg+h are initially concentrated but sediment as thermals ascend. Even
697 compared with the lifetime composite in Fig. 10, Qi+s are more stratified horizontally rather than
698 toward thermal cores, particularly from 3.5 km to 6.5 km, suggesting entrainment of Qi+s within
699 thermals at these altitudes. Simultaneously, Qc and Qr decrease while Qg+h increases at these
700 altitudes. Because wet growth (ice collecting supercooled liquid) is the primary graupel growth
701 process within 4ICE microphysics in the GCE (Lang et al. 2014), the droplet-loaded thermal
702 penetration toward ice layers appears to be the important graupel/hail generation process within
703 tropical deep convection.

704

705 **4. Conclusion: Thermal-driven Convection Invigoration Process**

706

707 We have investigated seasonal differences of the measured and simulated V_{dop} between the dry
708 and wet seasons to confirm dry-season convective vigor associated with enhanced cold
709 precipitation (graupel and hail) processes. Tracked thermal properties from the selected case
710 studies reveal unique updraft microphysics processes in the convective core that explain the dry-
711 wet contrast in deep convection. To summarize our findings in graupel-hail development
712 sequences, a thermal-driven process is proposed in the following steps (Fig. 12a).

713

714   1. Where condensation may occur within moist turbulent structures in the lower atmosphere,
715   local moist thermals may be initiated, which are characterized by dipole vortex rings with
716   intense vertical velocity, supersaturation, cloud droplets, and raindrops around the thermal
717   core.
718   2. When moist thermals penetrate the 0°C isothermal layer and dissipate in the mixed-phase
719   zone, cloud droplets are detrained and gradually glaciated to form ice-particle layers.
720   3. As additional thermals fill with droplets at the thermal core and penetrate the glaciated
721   mixed-phase zone, they entrain ice particles and collide with each other, generating graupel
722   and hail embryos.

4. Once graupel and hail particles grow sufficiently large, they start falling out from thermals and develop further by collecting supercooled droplets and ice particles during sedimentation.

The process of generating ice layers (Step 3) could be the largest source of uncertainty in this study. To prove the convective vigor process, this study used the simple bulk single-moment microphysics parameterization (Lang et al. 2014, Tao et al. 2016). This parameterization tends to convert droplets into ice particles through the saturation adjustment process. Cloud droplets are glaciated much more quickly when compared to two-moment microphysics (e.g. Matsui et al. 2023). Time series as well as altitude reference composite also shows some ice generation within the thermal core in later lifecycle stages (~10 km altitude), which may be associated with the Bergeron process. Yet, ice crystal formation processes remain one of the largest sources of microphysics uncertainty (Kanji et al. 2017; Korolev and Leisner 2020) and need further investigation to establish with adequate parameterizations. Furthermore, updrafts passing through the melting layer containing both large drops and ice crystals (which are identified here as a source of graupel) have also been pinpointed as a leading source of secondary ice production in oceanic convection sampled extensively via aircraft (Korolev et al. 2020). Thus, all quantitative components of the proposed ice-graupel generation process described here remain uncertain and subject to future investigations via instrumental observations and more detailed numerical simulations.

Nonetheless, building on the ability of existing knowledge and simulations to reproduce some basic features of observations during GoAmazon, Fig. 12b shows a newly proposed process that can explain why dry-season convection has more graupel and intense precipitation than wet-season counterparts in the following steps.

1. Dry-case (wet-case) convection tends to generate more (less) numbers of droplet-loaded thermals from the lower atmosphere because of larger potential buoyant energy at a low level in the dry season.

2. Once an ice layer is built from initial cumulus thermal ensembles (Fig. 11a), more (less) numbers of droplet-loaded thermals penetrate ice layers to generate more (less) graupel and hail embryos in dry-case (wet-case) convection.

3. Individual dry-case (wet-case) thermals can rise to higher (lower) elevations via weaker (stronger) dilution with faster (slower) updraft, elevating in-thermal graupel at higher (lower) altitudes.

4. During sedimentation, graupel in dry-case (wet-case) thermals has a higher (lower) chance to grow due to the longer (shorter) distance toward the melting level.

These new processes are proposed from the "golden" cases from the dry and wet seasons. Further investigation with more case studies will augment our hypothesis in the future.

The "hotter" surface in the dry season must be the physical origin of step 1, similar to L-O contrast (William and Stanfill, 2002). The dry season typically has clearer skies, less soil moisture, and stronger surface heating, leading to more turbulent heat flux and energy at the lower troposphere even during GoAmazon experiment (Biscaro et al., 2021; Ghate and Kollias, 2016). In contrast, the wet season is characterized by frequent precipitation and increased release of atmospheric latent heat with the weak surface sensible heat flux caused by wet soil moisture (Rocha et al., 2004). As a result, the entire troposphere experiences upward motion during the wet season, unlike its dry season counterpart (Tang et al., 2016).

Contrary to the speculation made by William and Stanfill (2002), it has been found that stronger surface heating and deeper PBL during the dry season do not increase the thermal "size" based on the classic similarity theory of Morton et al. (1956). Instead, our analysis of simulations indicates that the numbers and updraft velocity profiles of cumulus thermals become more important, particularly those initiated in the lower troposphere. Even for similar CAPE, the concentration of potential buoyancy profiles in the lower troposphere can trigger more vigorous convection. This is similar to the difference between mid-latitude continental and tropical maritime environments, where the mid-latitude continental environment tends to have more potential buoyancy in the mid-to-lower troposphere, leading to continental convective vigor (Matsui et al., 2020). For this, we need to investigate boundary layer dry thermals and deep-convective moist thermal seamlessly between various continental and maritime environments.

It is also hypothesized that the low-altitude concentrated cumulus thermal trains could additionally enhance the cold precipitation process by improving the residence time of graupel and hail within

785 the mixed-phase zone if thermal-spilled graupel and hail encounter subsequent new cumulus
786 thermals. Previous trajectory modeling (Heymsfield 1983) also suggested a similar mechanism for
787 enhancing graupel and hail residence time and growth by multiple convective cores. Heymsfield
788 (1983) used the multi-Doppler technique to generate a three-dimensional wind field, but it needed
789 more spatio-temporal resolution to characterize cumulus thermal. However, a stronger updraft core
790 mentioned in his study must be cumulus thermals. This investigation further requires a more
791 complex set of numerical simulations in the future.

792

793 The proposed thermal-driven invigoration process is based solely on thermodynamics and does
794 not consider aerosols' effect on deep convection, as demonstrated by previous studies over the
795 Amazon (William et al. 2002, Lin et al. 2006). Our choice of single-moment microphysics does
796 not consider the variability of background aerosols to initiate cloud droplets. However, this simple
797 microphysics can generate a fundamental dry-wet contrast characterized by the V_{dop} statistics. This
798 suggests that thermodynamics is the primary factor determining convective vigor, while aerosols
799 may have a significant but secondary role in invigorating convection (Matsui et al. 2020). Future
800 studies will require a higher-order moment of microphysics scheme to examine the impact of
801 aerosols on droplet and primary ice nucleation in thermals to confirm our hypothesis that dry-wet
802 aerosol contrast plays a secondary role.

803

804 It is well known that severe hailstorms and large hails are more frequently observed over the central
805 plains of North and South America (Liu and Zipser 2015, Bang and Cecil 2019). The hailstorms
806 in these regions are often associated with supercells, and mesocyclones play a crucial role in the
807 growth of very large hail by enhancing the residence time of the hails within the mixed-phase zone
808 (e.g., Nelson 1983; Ziegler et al. 1983). However, it is not known how a mesocyclone affects
809 thermal-like or plume-like updraft characteristics (Morrison et al., 2020), though satellites have
810 captured thermal chain-like periodic overshooting signals at the top of the supercells (Borque et
811 al. 2020). Thus, further observational and modeling investigations are required for the mid-latitude
812 regions to determine whether our proposed graupel/hail generation mechanisms can be applied.

813

814 The proposed process for graupel-hail generation and convective vigor is a time-dependent,
815 sequential, coupled dynamics-microphysics process. Although the traditional plume-based mass

816   flux scheme has been successful in representing the moist convection process in climate models
817   (e.g., Arakawa and Schubert 1974), our proposed convective microphysics process is not linear
818   and cannot be adequately represented by the traditional convective mass flux method. To represent
819   this process, thermal chain concepts with detailed microphysics processes must be introduced in
820   the parameterization for large-scale models (Morrison et al., 2020). Fine-resolution simulations
821   produce better continental convective vigor because they can resolve thermal dynamics and
822   microphysics (Robinson et al., 2011; Matsui et al., 2020). The mean radius of the tracked thermal
823   in this study, conducted using a 200 m mesh LES, is around 1 km, with a maximum size of around
824   2 km, which is comparable to the LES study using a 65-m horizontal grid spacing (Hernandez-
825   Deckers and Sherwood, 2016). However, due to the effective resolution being 5-10 times the actual
826   grid spacing, cumulus thermals, and graupel-hail generation processes are difficult to resolve for
827   storm-resolving models and perhaps any coarser Eulerian-type numerical atmospheric models
828   (Matsui et al., 2016). Conducting LES for regional and global weather and climate models is
829   impractical in the foreseeable future. Therefore, new types of dynamics-microphysics-coupled
830   cumulus thermal parameterization should be developed to better represent deep convection for
831   storm-resolving and coarse-resolution weather and climate models.

832

833   New ground-based Doppler phased array radar (PAR) technology (Kollias et al. 2022b) or multi-
834   Doppler agile scans (Kollias et al. 2022a) hold promise in observing and characterizing cumulus
835   thermals. Emerging PAR instruments have started capturing storm motion and microphysical
836   details at spatial and temporal resolutions akin to those seen in LES output (e.g. Takahashi et al.
837   2019, Kikuchi et al. 2020). These new observational capabilities are necessary for refining the
838   dynamics and microphysics in LESs, particularly in elucidating the process behind thermal-driven
839   convective vigor. Moreover, the advent of vertical motion estimates from high-resolution space-
840   based radars [EarthCARE, Wehr et al. 2023; Investigation of Convective Updrafts (INCUS),
841   https://incus.colostate.edu; the Atmosphere Observing System (AOS), https://aos.gsfc.nasa.gov)
842   will soon enable the global mapping of convective updrafts. These new satellite radar
843   measurements will generate a comprehensive global catalog detailing convective vigor and the
844   speed of intense thermals.

845

846 **Code Availability.** The GCE LES code, G-SDSU simulator code, and Python plotting codes used

847 in this manuscript are all available in the NCCS Data Portal

848 (https://portal.nccs.nasa.gov/datashare/cloudlibrary/PUB_DATA/GoAmazon_ACP/Code/).

849

850 **Data Availability.** The RWP measurements and VARNAL LSF data were available from the

851 Atmospheric Radiation Measurement (ARM) ARM Data Discovery

852 (https://adc.arm.gov/discovery/#/). These data were obtained from the ARM Mobile Facility

853 (AMF) at Manacapuru, Amazonas, Brazil, funded by A. U.S. Department of Energy (DOE) Office

854 of Science User Facility managed by the Biological and Environmental Research program. The

855 analysis data used in this manuscript is also available in the NCCS Data Portal

856 (https://portal.nccs.nasa.gov/datashare/cloudlibrary/PUB_DATA/GoAmazon_ACP/Data/)

857

858 **Author contribution.** T. Matsui designed and performed the GCE LESs, the V_{dop} forward

859 simulation, and the thermal tracking. D. Hernandez-Deckers developed the thermal tracking and

860 analysis code for the GCE LESs and prepared the V_{dop} figures for the thermal analysis. S.

861 Giangrande and T. Biscaro prepared RWP V_{dop} analysis. T. Matsui prepared the manuscript with

862 contributions from all co-authors.

863

864 **Competing interests.** At least one of the (co-)authors is a member of the editorial board of

865 Atmospheric Chemistry and Physics.

866

867 **Acknowledgments.** This project is funded by the NASA CloudSat and CALIPSO Science Team

868 (CCST) program (program manager: Dr. David Considine, grant number: 80NSSC21K1135). The

869 development of GCE is funded by the NASA GSFC Strategic Science resources (Associate

870 Director for Institutional Planning and Operation: Dr. Karen Mohr). We also thank the NASA

871 Advanced Supercomputing (NAS) Division and Center for Climate Simulation (NCCS) (Project

872 Manager T. Lee at NASA HQ) for providing the computational resources to conduct the GCE and

873 G-SDSU simulations, thermal tracking analysis, and stored model outputs. The authors thank an

874 anonymous reviewer for improving the manuscript.

875

References

876

877 Arakawa, A. and Schubert, W. H. (1974): Interaction of a cumulus cloud ensemble with the

878   large–scale environment, Part I, J. Atmos. Sci., 31, 674–701.

879 Bang, S. D., and D. J. Cecil, 2019: Constructing a Multifrequency Passive Microwave Hail

880   Retrieval and Climatology in the GPM Domain. J. Appl. Meteor. Climatol., 58, 1889–

881   1904, https://doi.org/10.1175/JAMC-D-19-0042.1.

882 Biscaro, T. S., Machado, L. A. T., Giangrande, S. E., and Jensen, M. P. (2021): What drives

883   daily precipitation over the central Amazon? Differences observed between wet and dry

884   seasons, Atmos. Chem. Phys., 21, 6735–6754, https://doi.org/10.5194/acp-21-6735-2021.

885 Blyth, A. M., S. G. Lasher-Trapp, and W. A. Cooper (2005): A study of thermals in cumulus

886   clouds, Quarterly Journal of the Royal Meteorological Society, 131, 1171–1190,

887   https://doi.org/10.1256/qj.03.180.

888 Borque, P., Vidal, L., Rugna, M., Lang, T. J., Nicora, M. G., & Nesbitt, S. W. (2020). Distinctive

889   Signals in 1-min Observations of Overshooting Tops and Lightning Activity in a Severe

890   Supercell Thunderstorm. *Journal of Geophysical Research: Atmospheres*, *125*(20),

891   e2020JD032856. https://doi.org/10.1029/2020JD032856

892 Chou, M.-D. and Suarez, M. J. (1999): A solar radiation parameterization for atmospheric

893   studies, NASA Tech. Rep. NASA/TM-1999-10460, vol 15, p 38,

894   https://ntrs.nasa.gov/archive/nasa/casi.ntrs.nasa.gov/19990060930.pdf.

895 Chou, M.-D. and Suarez, M. J. (2001): A thermal infrared radiation parameterization for

896   atmospheric studies, NASA/TM-2001-104606, vol 19, p 55,

897   https://ntrs.nasa.gov/archive/nasa/casi.ntrs.nasa.gov/20010072848.pdf.

898   Dolan, B., B. Fuchs, S. A. Rutledge, E. A. Barnes, and E. J. Thompson (2018): Primary Modes

899   of Global Drop Size Distributions, J. Atmos. Sci., 75, 1453–1476,

900   https://doi.org/10.1175/JAS-D-17-0242.1.

901   Emanuel, K. A., David Neelin, J., and Bretherton, C. S. (1994): On large-scale circulations in

902   convecting atmospheres, Q. J. R. Meteorol. Soc., 120, 1111–1143,

903   https://doi.org/10.1002/qj.49712051902.

904   Ghate, V. P. and Kollias, P. (2016): On the Controls of Daytime Precipitation in the Amazonian

905   Dry Season, J. Hydrometeor., 17, 3079–3097, https://doi.org/10.1175/JHM-D-16-

906   0101.1.

907   Giangrande, S. E., Biscaro, T. S., and Peters, J. M. (2023): Seasonal controls on isolated

908   convective storm drafts, precipitation intensity, and life cycle as observed during

909   GoAmazon2014/5, Atmospheric Chemistry and Physics, 23, 5297–5316,

910   https://doi.org/10.5194/acp-23-5297-2023.

911   Giangrande, S. E., Feng, Z., Jensen, M. P., Comstock, J. M., Johnson, K. L., Toto, T., Wang, M.,

912   Burleyson, C., Bharadwaj, N., Mei, F., Machado, L. A. T., Manzi, A. O., Xie, S., Tang,

913   S., Silva Dias, M. A. F., de Souza, R. A. F., Schumacher, C., and Martin, S. T. (2017):

914   Cloud characteristics, thermodynamic controls and radiative impacts during the

915   Observations and Modeling of the Green Ocean Amazon (GoAmazon2014/5)

916   experiment, Atmospheric Chemistry and Physics, 17, 14519–14541,

917   https://doi.org/10.5194/acp-17-14519-2017.

918   Giangrande, S. E., Toto, T., Jensen, M. P., Bartholomew, M. J., Feng, Z., Protat, A., Williams, C.

919   R., Schumacher, C., and Machado, L. (2016): Convective cloud vertical velocity and

920   mass-flux characteristics from radar wind profiler observations during GoAmazon2014/5,

Journal of Geophysical Research: Atmospheres, 121, 12,891–12,913,

https://doi.org/10.1002/2016JD025303.

Giangrande, S. E., Wang, D., and Mechem, D. B. (2020): Cloud regimes over the Amazon

Basin: perspectives from the GoAmazon2014/5 campaign, Atmospheric Chemistry and

Physics, 20, 7489–7507, https://doi.org/10.5194/acp-20-7489-2020.

Giangrande, S. E., E. P. Luke, and P. Kollias (2012): Characterization of Vertical Velocity and

Drop Size Distribution Parameters in Widespread Precipitation at ARM Facilities,

Journal of Applied Meteorology and Climatology, 51, 380–391,

https://doi.org/10.1175/JAMC-D-10-05000.1.

Giangrande, S. E., S. Collis, J. Straka, A. Protat, C. Williams, and S. Krueger (2013): A

Summary of Convective-Core Vertical Velocity Properties Using ARM UHF Wind

Profilers in Oklahoma, Journal of Applied Meteorology and Climatology, 52, 2278–2295,

https://doi.org/10.1175/JAMC-D-12-0185.1.

Grabowski, W. W. & Petch, Jon (2009): Deep Convective Clouds. Clouds in the Perturbed

Climate System: Their Relationship to Energy Balance. 2. 197-215,

https://doi.org/10.7551/mitpress/9780262012874.003.0009.

Gu, J.-F., Plant, R. S., Holloway, C. E., and Muetzelfeldt, M. R. (2020): Pressure drag for

shallow cumulus clouds: From thermals to the cloud ensemble, Geophysical Research

Letters, 47, e2020GL090460, https://doi.org/10.1029/2020GL090460.

Hartmann, D. L. (2016): Global Physical Climatology, 2nd ed., Academic Press, Cambridge,

UK, ISBN: 978-0-12-328531-7, DOI: https://doi.org/10.1016/C2009-0-00030-0.

942   Hernandez-Deckers, D. and Sherwood, S. C. (2016): A Numerical Investigation of Cumulus

943   Thermals, Journal of the Atmospheric Sciences, 73, 4117–4136, DOI: 10.1175/JAS-D-

944   15-0385.1.

945   Hernandez-Deckers, D. and Sherwood, S. C. (2018): On the Role of Entrainment in the Fate of

946   Cumulus Thermals, Journal of the Atmospheric Sciences, 75, 3911–3924, DOI:

947   10.1175/JAS-D-18-0077.1.

948   Hernandez-Deckers, D., Matsui, T., and Fridlind, A. M. (2022): Updraft dynamics and

949   microphysics: On the added value of the cumulus thermal reference frame in simulations

950   of aerosol-deep convection interactions, Atmospheric Chemistry and Physics, 22(2), 711–

951   724, DOI: 10.5194/acp-22-711-2022.

952   Heymsfield, A. J. (1983): Case Study of a Halistorm in Colorado. Part IV: Graupel and Hail

953   Growth Mechanisms Deduced through Particle Trajectory Calculations, J. Atmos. Sci.,

954   40, 1482–1509, https://doi.org/10.1175/1520-0469(1983)040<1482:CSOAHI>2.0.CO;2.

955   Holland, G. J., John, L., McBride, R. K., Smith, D. J., Jasper, D., and Keenan, T. D. (1986): The

956   BMRC Australian Monsoon Experiment: AMEX, Bulletin of the American

957   Meteorological Society, 67(12), 1466-1472, doi: 10.1175/1520-

958   0477(1986)067<1466:TBAMEA>2.0.CO;2.

959   Iguchi, T., Matsui, T., Tao, W., Khain, A., Phillips, V., Kidd, C., L'Ecuyer, T., Braun, S., and

960   Hou, A. (2014): WRF-SBM simulations of melting layer structure in mixed-phase

961   precipitation events observed during LPVEx, J. Appl. Meteor. Climatol., 53, 2710-2731,

962   doi:10.1175/JAMC-D-13-0334.1.

963   Jeyaratnam, J., Luo, Z. J., Giangrande, S. E., Wang, D., & Masunaga, H. (2021): A satellite-

964   based estimate of convective vertical velocity and convective mass flux: Global survey

965 and comparison with radar wind profiler observations, Geophysical Research Letters, 48,

966 e2020GL090675, https://doi.org/10.1029/2020GL090675.

967 Kanji, Z. A., Ladino, L. A., Wex, H., Boose, Y., Burkert-Kohn, M., Cziczo, D. J., & Krämer, M.

968 (2017): Overview of Ice Nucleating Particles, Meteorological Monographs, 58, 1.1–1.33,

969 DOI: 10.1175/AMSMONOGRAPHS-D-16-0006.1.

970 Keenan, T. D. and Carbone, R. E. (1992): A Preliminary Morphology of Precipitation Systems In

971 Tropical Northern Australia, Q.J.R. Meteorol. Soc., 118: 283-326,

972 https://doi.org/10.1002/qj.49711850406.

973 Kikuchi, H. et al. (2020): Initial observations for precipitation cores with X-band dual polarized

974 phased array weather radar, IEEE Transactions on Geoscience and Remote Sensing,

975 58(5), 3657-3666, http://doi.org/10.1109/TGRS.2019.2959628.

976 Kollias, P., Luke, E. P., Tuftedal, K., Dubois, M., & Knapp, E. J. (2022): Agile Weather

977 Observations using a Dual-Polarization X-band Phased Array Radar, 2022 IEEE Radar

978 Conference (RadarConf22), New York City, NY, USA, pp. 1-6, doi:

979 10.1109/RadarConf2248738.2022.9764308.

980 Kollias, P., Luke, E., Tuftedal, K., Dubois, M., & Knapp, E. J. (2022): Agile weather

981 observations using a dual-polarization X-band phased array radar, 2022 IEEE Radar

982 Conf., New York, NY, IEEE, 1–6,

983 https://doi.org/10.1109/RadarConf2248738.2022.9764308.

984 Kollias, P., & Coauthors (2022): Science Applications of Phased Array Radars, Bull. Amer.

985 Meteor. Soc., 103, E2370–E2390, https://doi.org/10.1175/BAMS-D-21-0173.1.

986 Korolev, A., Heckman, I., Wolde, M., Ackerman, A. S., Fridlind, A. M., Ladino, L. A., Lawson,

987 R. P., Milbrandt, J., and Williams, E. (2020): A new look at the environmental conditions

988   favorable to secondary ice production, Atmos. Chem. Phys., 20, 1391–1429,

989   https://doi.org/10.5194/acp-20-1391-2020.

990   Korolev, A. and Leisner, T. (2020): Review of experimental studies of secondary ice production,

991   Atmos. Chem. Phys., 20, 11767–11797, https://doi.org/10.5194/acp-20-11767-2020.

992   Lang, S. E., Tao, W.-K., Chern, J.-D., Wu, D., & Li, X. (2014): Benefits of a fourth ice class in

993   the simulated radar reflectivities of convective systems using a bulk microphysics

994   scheme, J. Atmos. Sci., 71, 3583–3612, https://doi.org/10.1175/JAS-D-13-0330.1.

995   Lin, J. C., Matsui, T., Pielke Sr., R. A., & Kummerow, C. (2006): Effects of biomass burning-

996   derived aerosols on precipitation and clouds in the Amazon Basin: A satellite-based

997   empirical study, Journal of Geophysical Research, 111, D19204,

998   doi:10.1029/2005JD006884.

999   Liu, C., & Zipser, E. J. (2015). The global distribution of largest, deepest, and most intense

1000   precipitation systems. *Geophysical Research Letters*, *42*(9), 3591-3595.

1001   https://doi.org/10.1002/2015GL063776

1002   Lucas, C., Zipser, E. J., & Lemone, M. A. (1994): Vertical velocity in oceanic convection off

1003   tropical Australia, J. Atmos. Sci., 51, 3183–3193, doi:10.1175/1520-

1004   0469(1994)051,3183: VVIOCO.2.0.CO;2.

1005   Martin, S. T., & Coauthors (2017): The Green Ocean Amazon Experiment (GoAmazon2014/5)

1006   Observes Pollution Affecting Gases, Aerosols, Clouds, and Rainfall over the Rain Forest,

1007   Bulletin of the American Meteorological Society, 98, 981–997, DOI: 10.1175/BAMS-D-

1008   15-00221.1.

1009   Matsui, T., & Mocko, D. M. (2014): Transpiration and Physical Evaporation: Regional and

1010   Seasonal Variability Over the Conterminous United States, In Encyclopedia of Natural

Resources, 1st Ed.; Wang, Y. Q., Ed.; Taylor & Francis Group: New York. 1086pp, ISBN 9781439852583 - CAT# K12418.

Matsui, T., & Coauthors (2014a): Current and Future Perspectives of Aerosol Research at NASA Goddard Space Flight Center, BAMS Meeting Summary 95, ES203–ES207, doi: http://dx.doi.org/10.1175/BAMS-D-13-00153.1.

Matsui, T., & Coauthors (2014b): Introducing multisensor satellite radiance-based evaluation for regional Earth System modeling, Journal of Geophysical Research, 119, 8450–8475, doi:10.1002/2013JD021424.

Matsui, T., & Coauthors (2016): On the land-ocean contrast of tropical convection and microphysics statistics derived from TRMM satellite signals and global storm-resolving models, Journal of Hydrometeorology, 17, 1425-1445, doi:10.1175/JHM-D-15-0111.1.

Matsui, T., & Coauthors (2018): Impact of Radiation Frequency, Precipitation Radiative Forcing, and Radiation Column Aggregation on Convection-Permitting West African Monsoon Simulations, Climate Dynamics, 1-21, https://doi.org/10.1007/s00382-018-4187-2.

Matsui, T., & Coauthors (2020): Polarimetric Radar Characteristics of Simulated and Observed Intense Convective Cores for a Midlatitude Continental and Tropical Maritime Environment, J. Hydrometeor., 21, 501–517, https://doi.org/10.1175/JHM-D-19-0185.1.

Matsui, T., & Coauthors (2023): Systematic validation of ensemble cloud-process simulations using polarimetric radar observations and simulator over the NASA Wallops Flight Facility, Journal of Geophysical Research: Atmospheres, 128, e2022JD038134, https://doi.org/10.1029/2022JD038134.

1032 Morrison, H., Peters, J. M., Varble, A. C., Hannah, W. M., & Giangrande, S. E. (2020). Thermal

1033   Chains and Entrainment in Cumulus Updrafts. Part I: Theoretical Description. Journal of

1034   the Atmospheric Sciences, 77, 3637–3660. [DOI: 10.1175/JAS-D-19-0243.1]

1035 Morrison, H., Jeevanjee, N., Lecoanet, D., & Peters, J. M. (2023). What controls the entrainment

1036   rate of dry buoyant thermals with varying initial aspect ratio?. Journal of the Atmospheric

1037   Sciences, [DOI: 10.1175/JAS-D-23-0063.1], in press.

1038 Morton, B. R., Taylor, G. I., & Turner, J. S. (1956): Turbulent gravitational convection from

1039   maintained and instantaneous sources. Proc. Roy. Soc. London, 234A, 1–23,

1040   https://doi.org/10.1098/RSPA.1956.0011.

1041 Nelson, S. P., 1983: The influence of storm flow structure on hail growth. *J. Atmos. Sci.*, 40,

1042   1965–1983, https://doi.org/10.1175/1520-0469(1983)040<1965:TIOSFS>2.0.CO;2.

1043 Öktem, R., Romps, D. M., & Varble, A. C. (2023). No Warm-Phase Invigoration of Convection

1044   Detected during GoAmazon. Journal of the Atmospheric Sciences, 80, 2345–2364. [DOI:

1045   10.1175/JAS-D-22-0241.1]

1046 Peters, J. M., Morrison, H., Varble, A. C., Hannah, W. M., & Giangrande, S. E. (2020). Thermal

1047   Chains and Entrainment in Cumulus Updrafts. Part II: Analysis of Idealized Simulations.

1048   Journal of the Atmospheric Sciences, 77, 3661–3681. [DOI: 10.1175/JAS-D-19-0244.1]

1049 Pielke, R. A. (2001). Influence of the spatial distribution of vegetation and soils on the prediction

1050   of cumulus convective rainfall. Rev. Geophys., 39, 151–177,

1051   doi:10.1029/1999RG000072.

1052 Pope, M., Jakob, C., & Reeder, M. J. (2009). Regimes of the North Australian Wet Season.

1053   Journal of Climate, 22, 6699–6715. [DOI: 10.1175/2009JCLI3057.1]

1054 Prein, A. F., Ge, M., Valle, A. R., Wang, D., & Giangrande, S. E. (2022). Towards a unified

1055   setup to simulate mid-latitude and tropical mesoscale convective systems at kilometer-

1056   scales. Earth and Space Science, 9. [DOI: 10.1029/2022EA002295]

1057 Ramos-Valle, A. N., Prein, A. F., Ge, M., Wang, D., & Giangrande, S. E. (2023). Grid spacing

1058   sensitivities of simulated mid-latitude and tropical mesoscale convective systems in the

1059   convective gray zone. Journal of Geophysical Research: Atmospheres, 128. [DOI:

1060   10.1029/2022JD037043]

1061 Robinson, F., Sherwood, S., Gerstle, D., Liu, C., & Kirshbaum, D. (2011). Exploring the land-

1062   ocean contrast in convective vigor using islands. J. Atmos. Sci., 68, 602–618,

1063   https://doi.org/10.1175/2010JAS3558.1.

1064 Rocha, H. R., Goulden, M., Miller, S. D., Menton, M. C., Pinto, L. D. V. O., Freitas, H. C., &

1065   Figueira, A. M. S. (2004). Seasonality of water and heat fluxes over a tropical forest in

1066   eastern Amazonia. Ecol. Appl., 14, 22–32.

1067 Romps, D. M., & Charn, A. B. (2015). Sticky Thermals: Evidence for a Dominant Balance

1068   between Buoyancy and Drag in Cloud Updrafts. J. Atmos. Sci., 72, 2890–2901,

1069   https://doi.org/10.1175/JAS-D-15-0042.1.

1070 Sherwood, S. C., Hernández-Deckers, D., Colin, M., & Robinson, F. (2013). Slippery Thermals

1071   and the Cumulus Entrainment Paradox. Journal of the Atmospheric Sciences, 70, 2426–

1072   2442, [DOI: 10.1175/JAS-D-12-0220.1]

1073 Steiner, M., Houze Jr., R. A., & Yuter, S. E. (1995). Climatological characterization of three-

1074   dimensional storm structure from operational radar and rain gauge data. Journal of

1075   Applied Meteorology, 34, 1978–2007.

1076 Stephens, G. L., Vane, D. G., Boain, R. J., Mace, G. G., Sassen, K., Wang, Z., ... CloudSat

1077   Science Team (2002). The CloudSat mission and the A-Train: A new dimension of

1078   space-based observations of clouds and precipitation. Bull. Amer. Meteorol. Soc., 83,

1079   1771-1790, doi:10.1175/BAMS-83-12-1771.

1080 Stolz, D. C., Rutledge, S. A., & Pierce, J. R. (2015). Simultaneous influences of thermodynamics

1081   and aerosols on deep convection and lightning in the tropics. J. Geophys. Res. Atmos.,

1082   120, 6207–6231, https://doi.org/10.1002/2014JD023033.

1083 Sullivan, S. C., Voigt, A. (2021). Ice microphysical processes exert a strong control on the

1084   simulated radiative energy budget in the tropics. Commun Earth Environ 2, 137,

1085   https://doi.org/10.1038/s43247-021-00206-7

1086 Takahashi, H., Luo, Z. J., & Stephens, G. L. (2017). Level of neutral buoyancy, deep convective

1087   outflow, and convective core: New perspectives based on 5 years of CloudSat data.

1088   Journal of Geophysical Research: Atmospheres, 122(5), 2958-2969.

1089 Takahashi, H., Luo, Z. J., & Stephens, G. L. (2021). Revisiting the entrainment relationship of

1090   convective plumes: A perspective from global observations. Geophys. Res. Lett.,

1091   https://doi.org/10.1029/2020GL092349

1092 Takahashi, N., et al. (2019). Development of multi-parameter phased array weather radar (MP-

1093   PAWR) and early detection of torrential rainfall and tornado risk. Journal of Disaster

1094   Research, 14(2), 235-247, http://doi.org/10.20965/jdr.2019.p0235

1095 Tang, S., Xie, S., Zhang, Y., Zhang, M., Schumacher, C., Upton, H., Jensen, M. P., Johnson, K.

1096   L., Wang, M., Ahlgrimm, M., Feng, Z., Minnis, P., and Thieman, M. (2016). Large-scale

1097   vertical velocity, diabatic heating and drying profiles associated with seasonal and diurnal

variations of convective systems observed in the GoAmazon2014/5 experiment. Atmos.

Chem. Phys., 16, 14249–14264, https://doi.org/10.5194/acp-16-14249-2016.

Tao, W.-K., Lang, S., Zeng, X., Li, X., Matsui, T., Mohr, K., Posselt, D., Chern, J., Peters-

Lidard, C., Norris, P. M., Kang, I.-S., Choi, I., Hou, A., Lau, K.-M., and Yang, Y.-M.

(2014). The Goddard Cumulus Ensemble model (GCE): improvements and applications

for studying precipitation processes. Atmospheric Research, 143, 392-424. doi:

http://dx.doi.org/10.1016/j.atmosres.2014.03.005.

Tao, W.-K., Wu, D., Lang, S., Chern, J.-D., Peters-Lidard, C., Fridlind, A., and Matsui, T.

(2016). High-resolution NU-WRF simulations of a deep convective-precipitation system

during MC3E: Further improvements and comparisons between Goddard microphysics

schemes and observations. J. Geophys. Res. Atmos., 121, 1278–1305,

https://doi.org/10.1002/2015JD023986.

Tao, K., Iguchi, T., Lang, S., Li, X., Mohr, K., Matsui, T., & Braun, S. (2022). Relating Vertical

Velocity and Cloud/Precipitation Properties: A Numerical Cloud Ensemble Modeling

Study of Tropical Convection. *Journal of Advances in Modeling Earth

Systems*, *14*(9), e2021MS002677. https://doi.org/10.1029/2021MS002677

Tokay, A., and Short, D. A. (1996). Evidence from Tropical Raindrop Spectra of the Origin of

Rain from Stratiform versus Convective Clouds. Journal of Applied Meteorology and

Climatology, 35, 355–371. [DOI: 10.1175/1520-

0450(1996)035<0355:EFTRSO>2.0.CO;2]

Wang, D., Giangrande, S. E., Bartholomew, M. J., Hardin, J., Feng, Z., Thalman, R., and

Machado, L. A. T. (2018). The Green Ocean: precipitation insights from the

1120   GoAmazon2014/5 experiment. Atmospheric Chemistry and Physics, 18, 9121–9145.

1121   [DOI: 10.5194/acp-18-9121-2018]

1122   Wang, D., Giangrande, S. E., Schiro, K., Jensen, M. P., & Houze, R. A. (2019). The

1123   characteristics of tropical and midlatitude mesoscale convective systems as revealed by

1124   radar wind profilers. Journal of Geophysical Research: Atmospheres, 124, 4601–4619.

1125   [DOI: 10.1029/2018JD030087]

1126   Wehr, T., Kubota, T., Tzeremes, G., Wallace, K., Nakatsuka, H., Ohno, Y., Koopman, R., Rusli,

1127   S., Kikuchi, M., Eisinger, M., Tanaka, T., Taga, M., Deghaye, P., Tomita, E., and

1128   Bernaerts, D. (2023). The EarthCARE mission – science and system overview. Atmos.

1129   Meas. Tech., 16, 3581–3608, https://doi.org/10.5194/amt-16-3581-2023.

1130   Williams, E., and Stanfill, S. (2002). The physical origin of the land–ocean contrast in lightning

1131   activity. C. R. Phys., 3, 1277–1292, doi:10.1016/S1631-0705(02)01407-X.

1132   Williams, E., Chan, T., and Boccippio, D. (2004). Islands as miniature continents: Another look

1133   at the land–ocean lightning contrast. J. Geophys. Res., 109, D16206,

1134   doi:10.1029/2003JD003833.

1135   Williams, E., Mushtak, V., Rosenfeld, D., Goodman, S., and Boccippio, D. (2005).

1136   Thermodynamic conditions favorable to superlative thunderstorm updraft, mixed phase

1137   microphysics and lightning flash rate. Atmos. Res., 76, 288–306,

1138   doi:10.1016/j.atmosres.2004.11.009.

1139   Williams, C. R., Barrio, J., Johnston, P. E., Muradyan, P., and Giangrande, S. E. (2023).

1140   Calibrating radar wind profiler reflectivity factor using surface disdrometer observations.

1141   Atmospheric Measurement Techniques, 16, 2381–2398. [DOI: 10.5194/amt-16-2381-

1142   2023]

1143 Wu, J., Del Genio, A. D., Yao, M.-S., and Wolf, A. B. (2009). WRF and GISS SCM simulations

1144    of convective updraft properties during TWP-ICE. Journal of Geophysical Research, 114,

1145    D04206. [DOI: 10.1029/2008JD010851]

1146 Xie, S., Cederwall, R. T., and Zhang, M. (2004). Developing long-term single-column

1147    model/cloud system–resolving model forcing data using numerical weather prediction

1148    products constrained by surface and top of the atmosphere observations. J. Geophys.

1149    Res., 109, D01104, doi:10.1029/2003JD004045.

1150 Xu, X., Sun, C., Lu, C., Liu, Y., Zhang, G. J., and Chen, Q. (2021). Factors affecting entrainment

1151    rate in deep convective clouds and parameterizations. Journal of Geophysical Research:

1152    Atmospheres, 126, e2021JD034881. [DOI: 10.1029/2021JD034881]

1153 Yanai, M., Esbensen, S., and Chu, J. (1973). Determination of Bulk Properties of Tropical Cloud

1154    Clusters from Large-Scale Heat and Moisture Budgets. J. Atmos. Sci., 30, 611–627,

1155    https://doi.org/10.1175/1520-0469(1973)030<0611:DOBPOT>2.0.CO;2.

1156 Yuter, S. E., and Houze Jr., R. A. (1995). Three-dimensional kinematic and microphysical

1157    evolution of Florida cumulonimbus. Part II: Frequency distribution of vertical velocity,

1158    reflectivity, and differential reflectivity. Monthly Weather Review, 123, 1941–1963.

1159 Zipser, E. J., Liu, C., Cecil, D. J., Nesbitt, S. W., and Yorty, D. P. (2006). Where are the most

1160    intense thunderstorms on Earth? Bull. Amer. Meteor. Soc., 87, 1057–1071,

1161    doi:10.1175/BAMS-87-8-1057.

1162 Zhang, M., and Lin, J. (1997). Constrained variational analysis of sounding data based on

1163    column-integrated budgets of mass, heat, moisture, and momentum: Approach and

1164    application to ARM measurements. J. Atmos. Sci., 54(11), 1503–1524,

1165    doi:10.1175/1520-0469(1997)054<1503:CVAOSD>2.0.CO;2.

1166   Zhang, M., Lin, J., Cederwall, R. T., Yio, J. J., and Xie, S. C. (2001). Objective analysis of ARM

1167   IOP data: Method and sensitivity. Mon. Weather Rev., 129(2), 295–311,

1168   doi:10.1175/1520-0493(2001)129<0295:OAOAID>2.0.CO;2.

1169   Ziegler, C. L., P. S. Ray, and N. C. Knight, 1983: Hail growth in an Oklahoma multicell storm. *J.*

1170   *Atmos. Sci.*, 40, 1768–1791, https://doi.org/10.1175/1520-

1171   0469(1983)040<1768:HGIAOM>2.0.CO;2.

1172
1173

1174
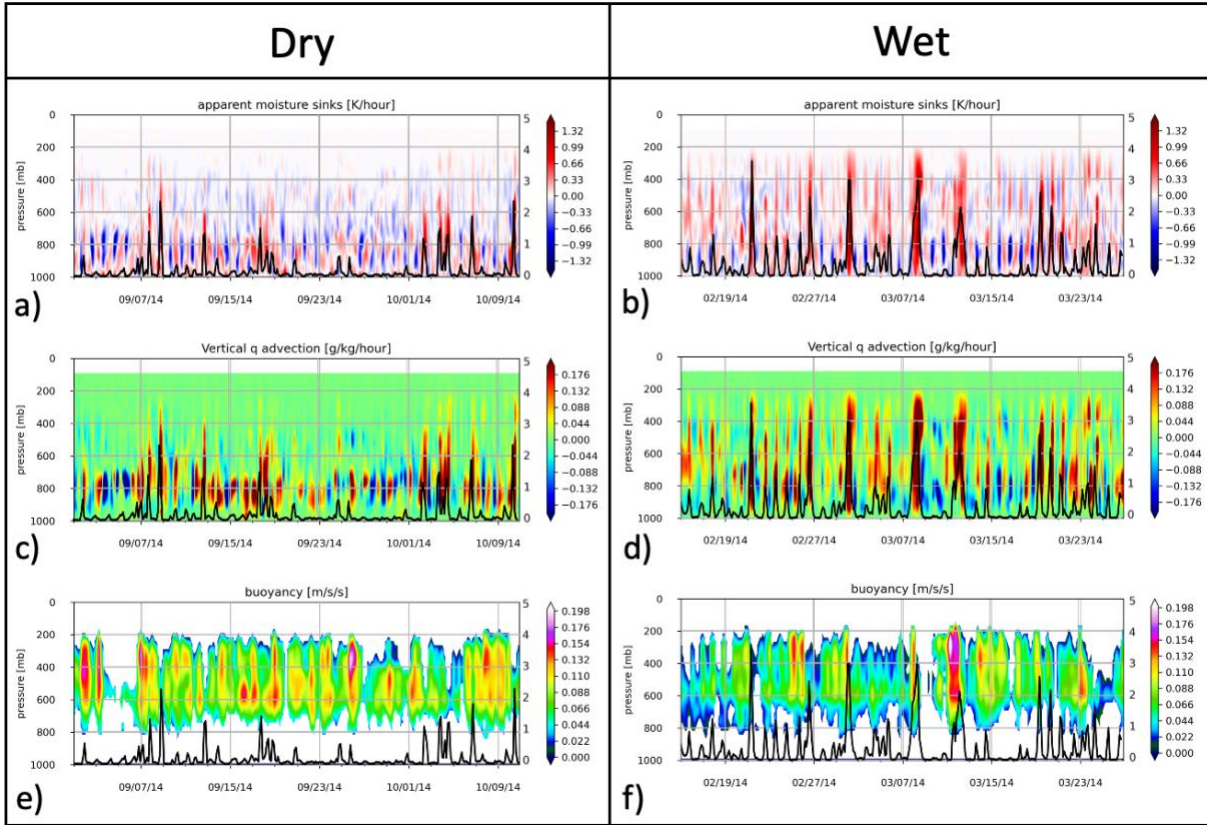
   Figures

1176

1177   Figure 1. Time series of VARNAL large-scale forcing profiles between wet and dry periods: (a-b)
1178   apparent moisture sink (Q2), (c-d) vertical moisture advection, (e-f) potential buoyancy. The black
1179   solid lines on the secondary y-axis represent the surface precipitation rate.
1180
1181
1182
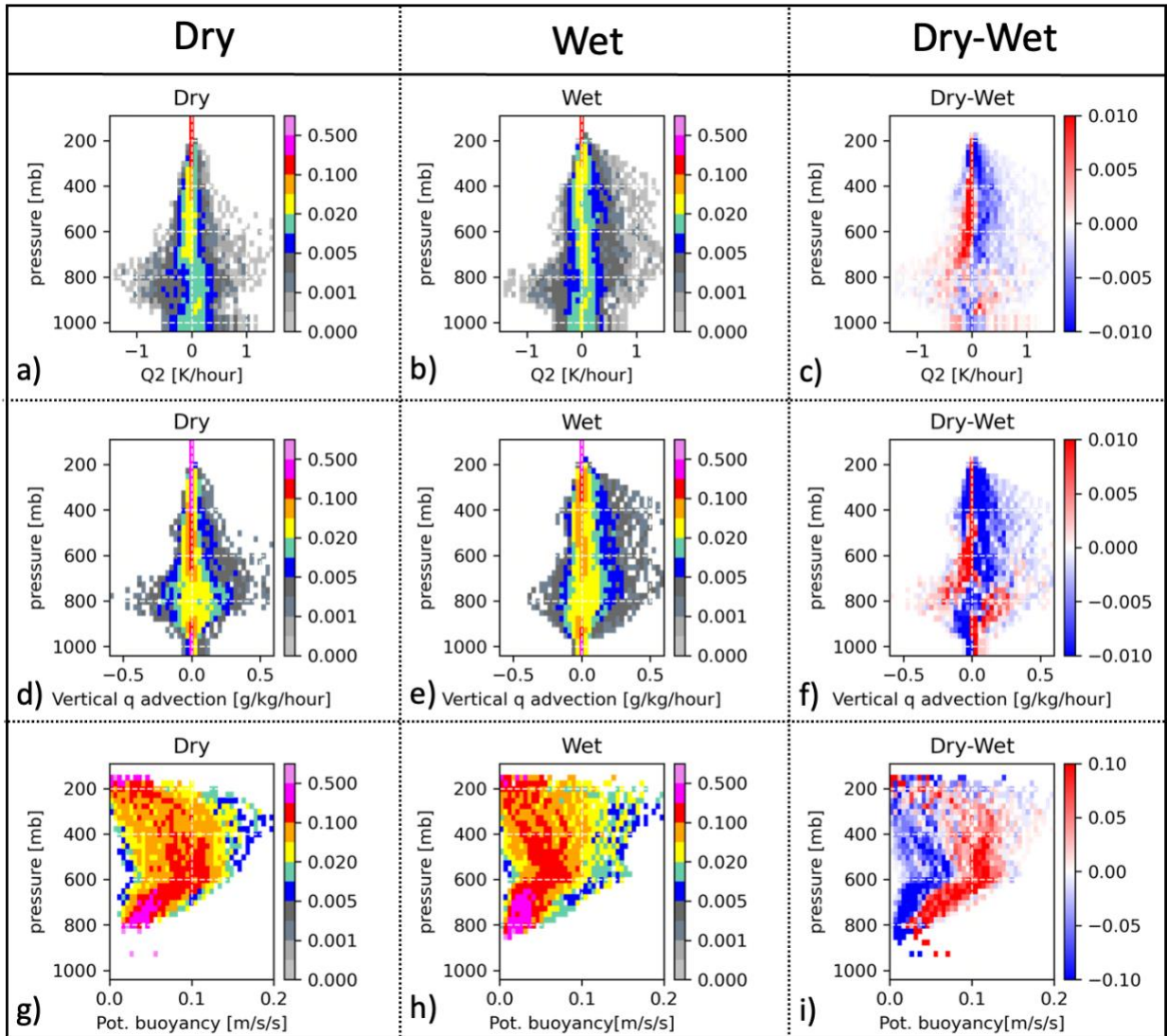
1183

1184 Figure 2. Contoured Frequency of Altitude Diagram (CFADs) of (a-c) apparent moisture sink (Q2),
1185 (d-f) vertical moisture (q) advection, (g-i) potential buoyancy integrated over dry and wet periods,
1186 as well as dry-wet differences.
1187
1188
1189

1190
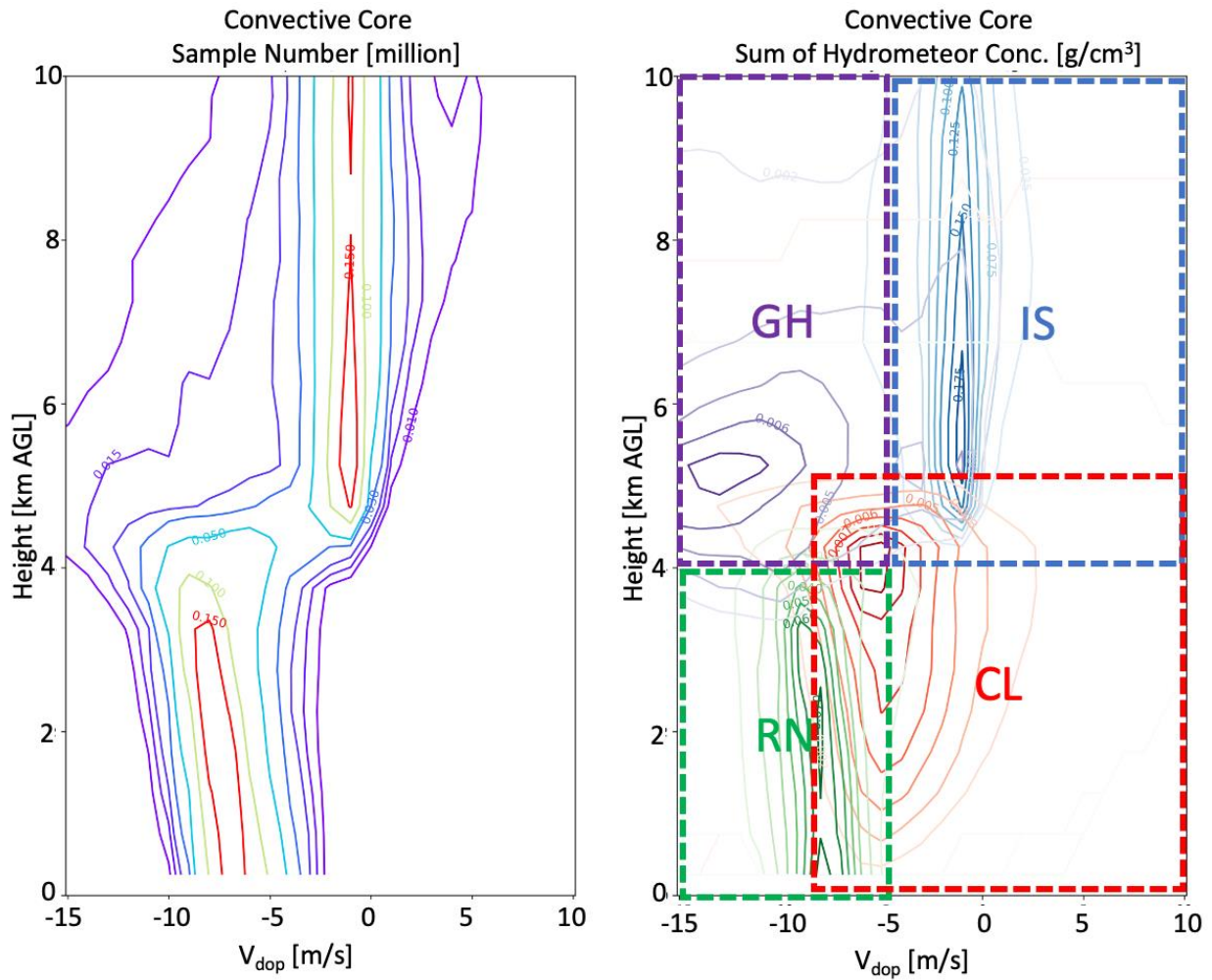
1191

1192   Figure 3. (a) Cumulative V_{dop} sample numbers from LESs during dry and wet periods, presented
1193   as CFADs for each V_{dop} bin and altitude. (b) the cumulative hydrometeor mass concentrations
1194   from each V_{dop}-altitude bin. Red contours represent "cloud (CL)", green contours represent "rain
1195   (RN)" blue contours represent "ice and snow (IS)", and purple contours represent "graupel and
1196   hail (GH)".

1197

1198

1199

1200
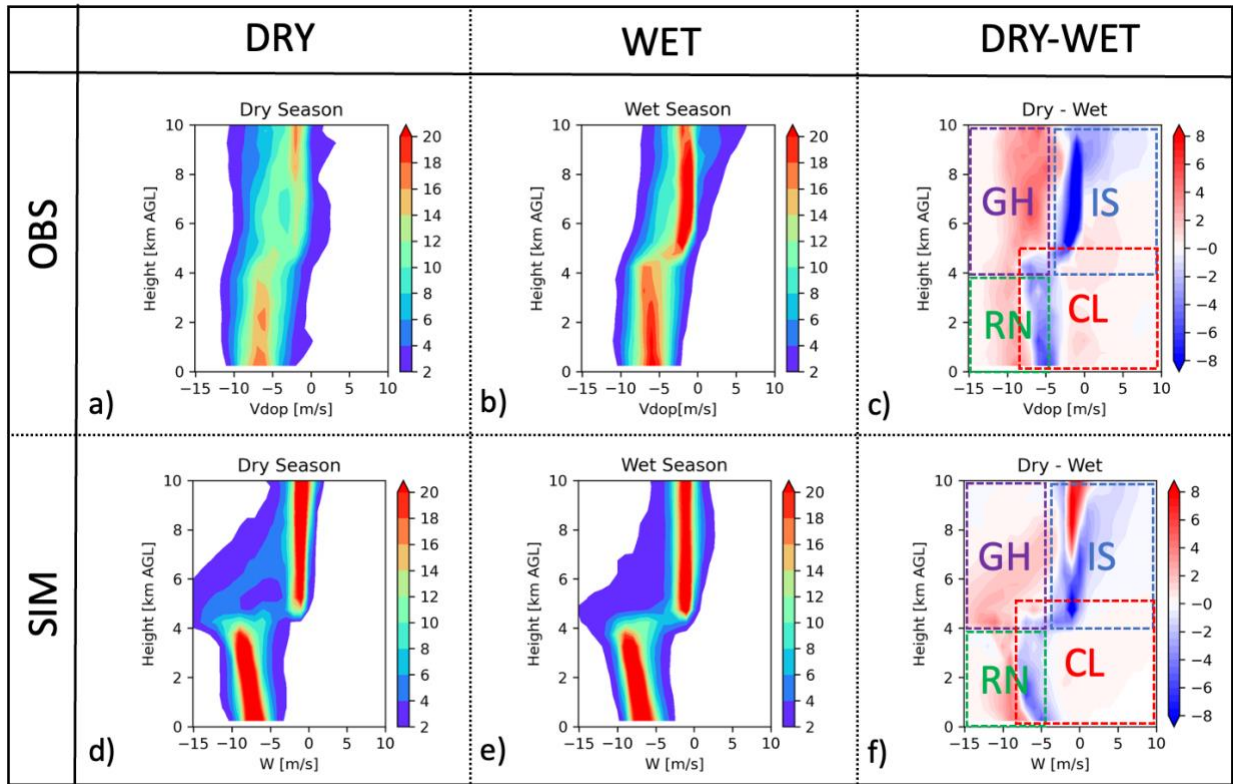
1201

1202 Figure 4. Contoured Frequency of Altitude Diagram (CFADs) of V_{dop} integrated over dry and wet
1203 periods, as well as dry-wet differences. The upper raw (a-c) represents observed composites, while
1204 the lower raw represents simulated composites. CL, RN, IS, and GH represent the hydrometeor
1205 regimes defined in Fig. 3.

1206

1207

1208
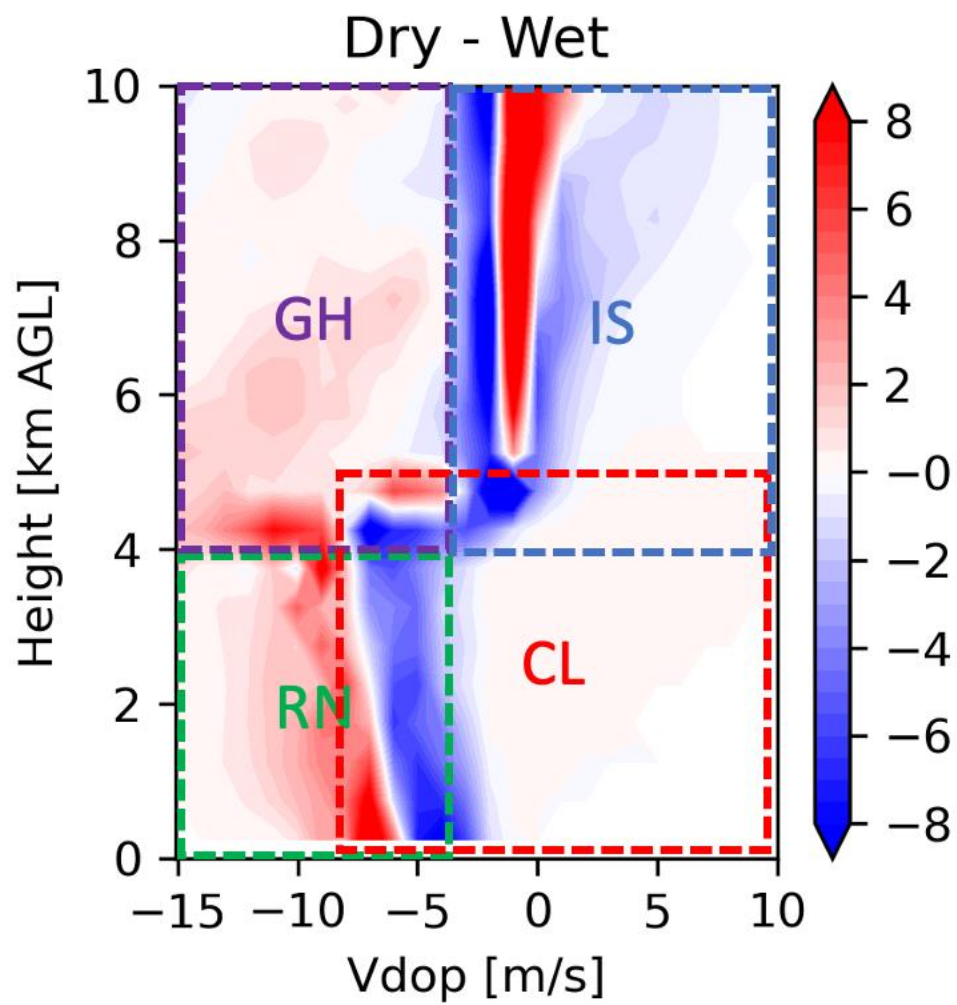
1209

1210   Figure 5. Contoured Frequency of Altitude Diagram (CFADs) of simulated V_{dop}, differentiated for
1211   dry- and wet-season golden cases.

1212

1213
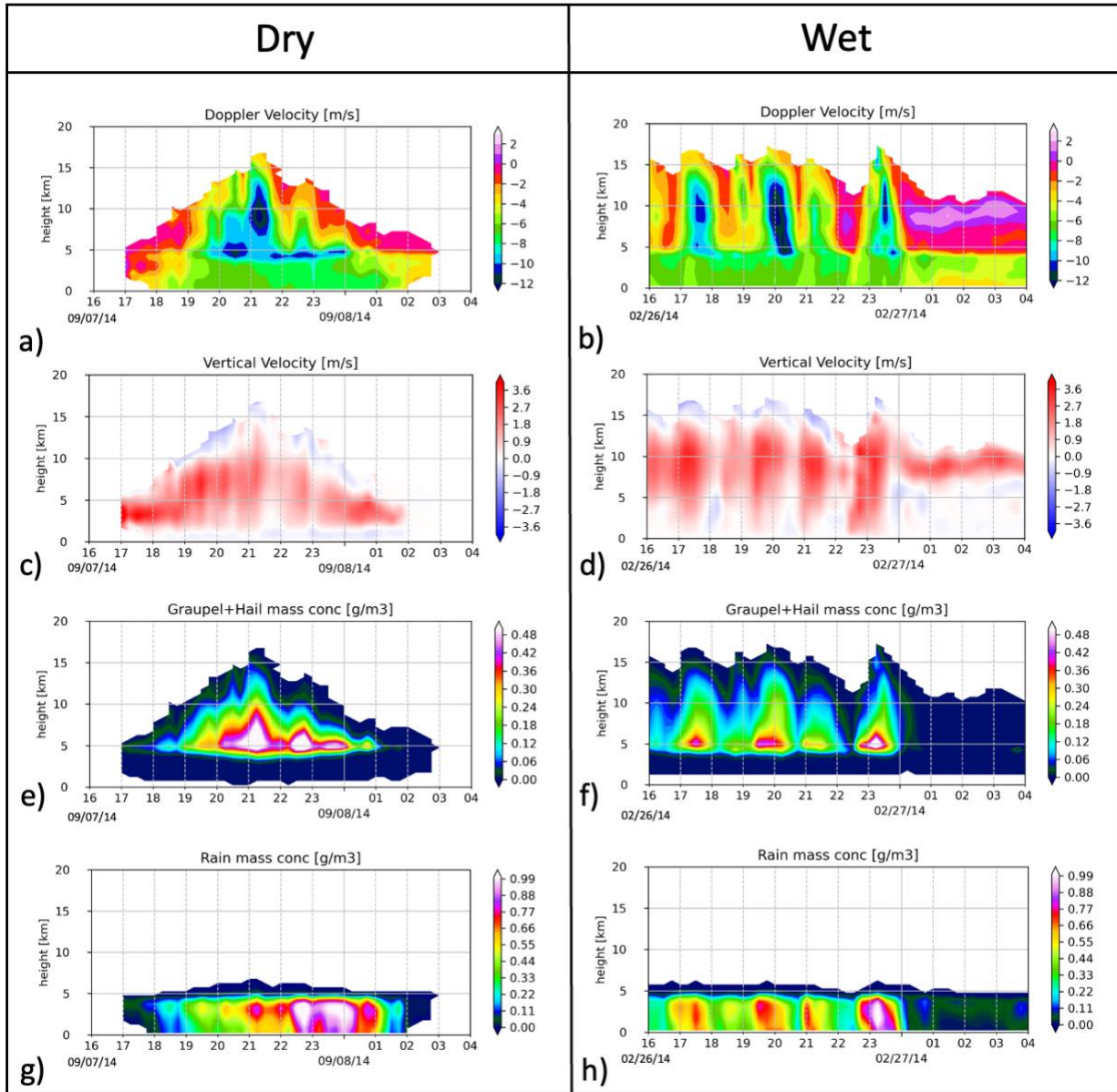
1214

1215 Figure 6. Time series of convective core-mean (a-b) Doppler velocity, (c-d) vertical velocity, (e-
1216 f) graupel and hail concentrations, and (g-h) rain concentrations profiles of convective grids from
1217 the dry- and wet-season golden cases.
1218

1219
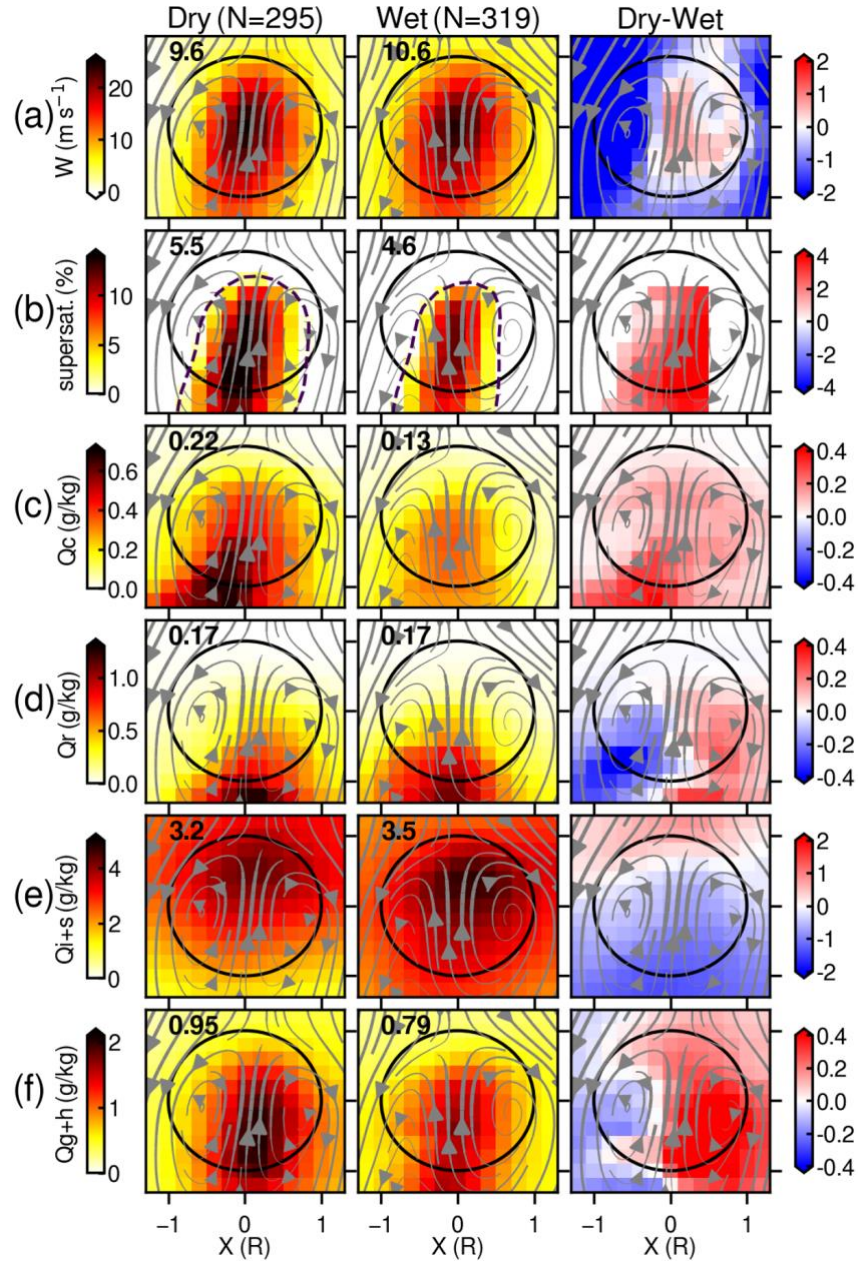
1220

Figure 7. Cross sections along the x-z plane of flux-weighted thermal values of (a) vertical velocity
(W), (b) supersaturation (S), (c) cloud droplet mass concentration (Qc), (d) rain mass concentration
(Qr), (e) ice and snow mass concentration (Qi+s), and (f) graupel and hail mass concentration
(Qg+h), for composites of all tracked thermals at the point of their maximum vertical velocity,
scaled by their radius (horizontal and vertical coordinates are in units of mean thermal radii). Left,
middle, and right column corresponds to the dry-season golden case, the wet-season golden case,
and dry-wet case difference, respectively. Upper left values in each panel are the flux- and radius-
weighted mean over all samples. Arrows indicate the average flow streamlines in the rising thermal
reference frame. The dashed contour in supersaturation values corresponds to 100% relative
humidity. These are reference-time (t=0) mean values.

1231

1232
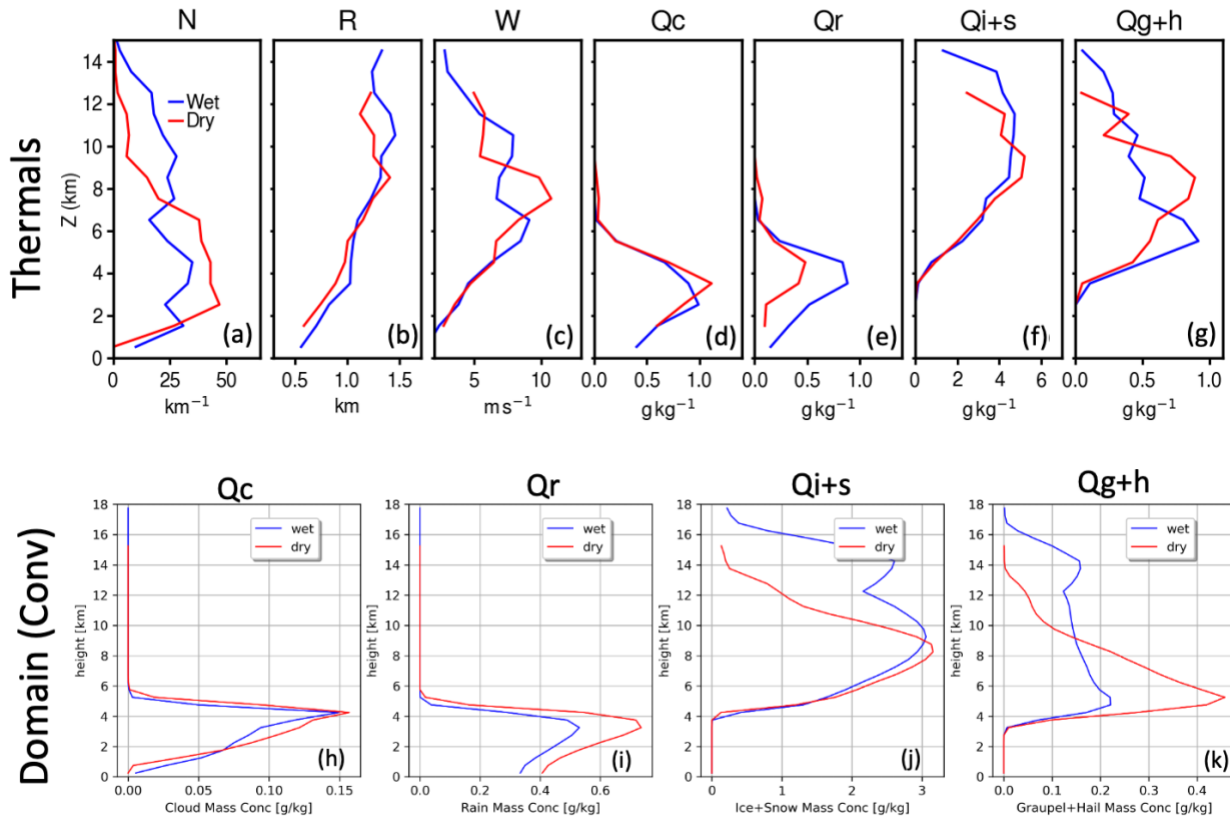
1233

1234 Figure 8. (a-f) Vertical profiles of thermal-mean (a) number concentrations (N), (b) radius (R), (c)
1235 vertical velocity (W), (d) cloud droplet mass concentration (Qc), (e) rain mass concentration (Qr),
1236 (f) ice and snow mass concentration (Qi+s), and (g) graupel and hail mass concentration (Qg+h).
1237 These are all-thermal mean values.
1238 (g-j) Vertical profile of domain-mean (h) cloud droplet mass concentration (Qc), (i) rain mass
1239 concentration (Qr), (j) ice and snow mass concentration (Qi+s), and (k) graupel and hail mass
1240 concentration (Qg+h)   of convective grids from the dry- and wet-season golden cases.
1241

1242
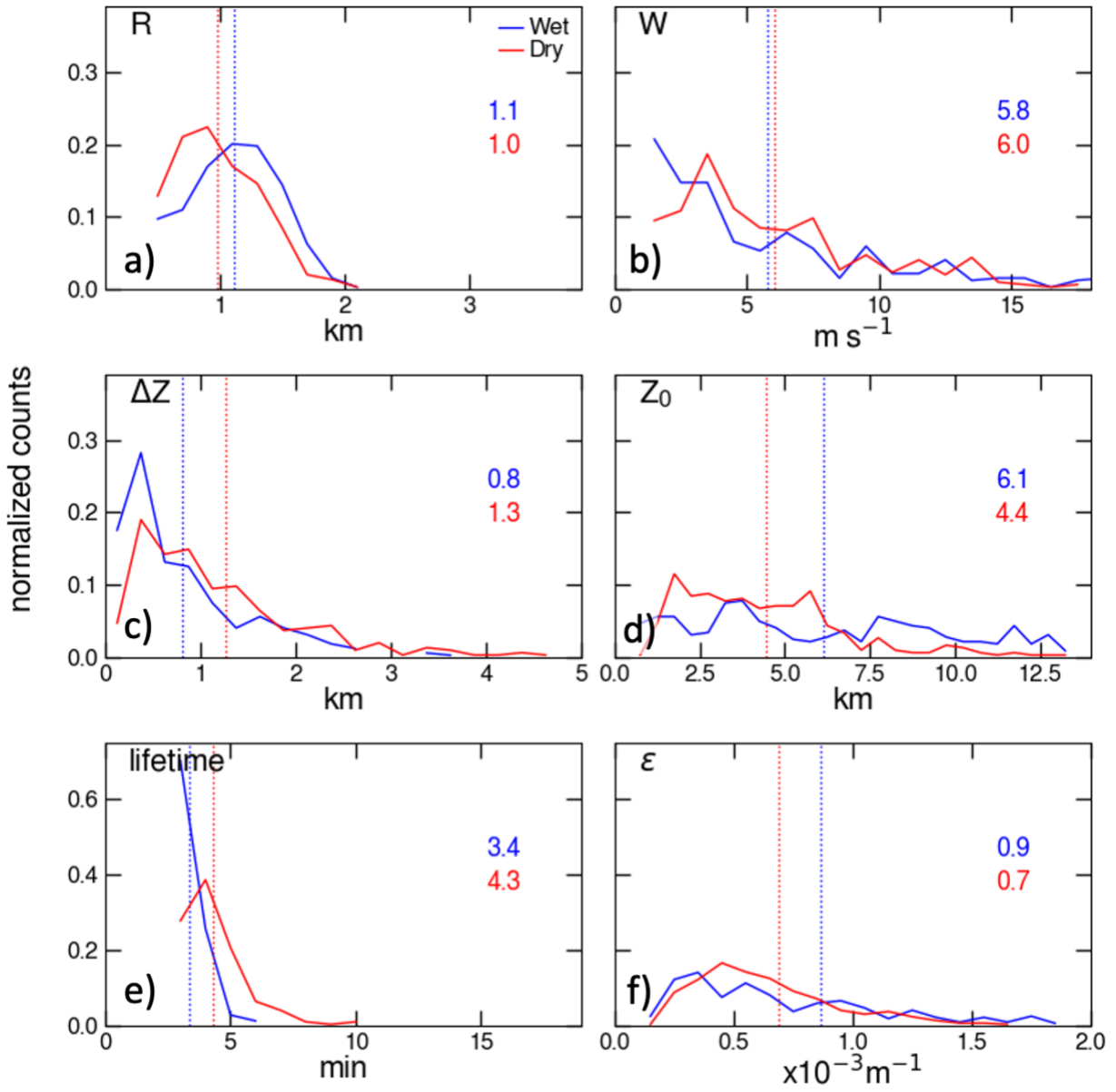
1243

1244 Figure 9. Normalized histogram of thermal (a) radii (R), (b) vertical velocity (W), (c) travel
1245 distance (ΔZ), (d) initiated level (Z_0), (e) lifetime, and (f) entrainment rate (ε) from the dry- and
1246 wet-season golden cases.

1247

1248
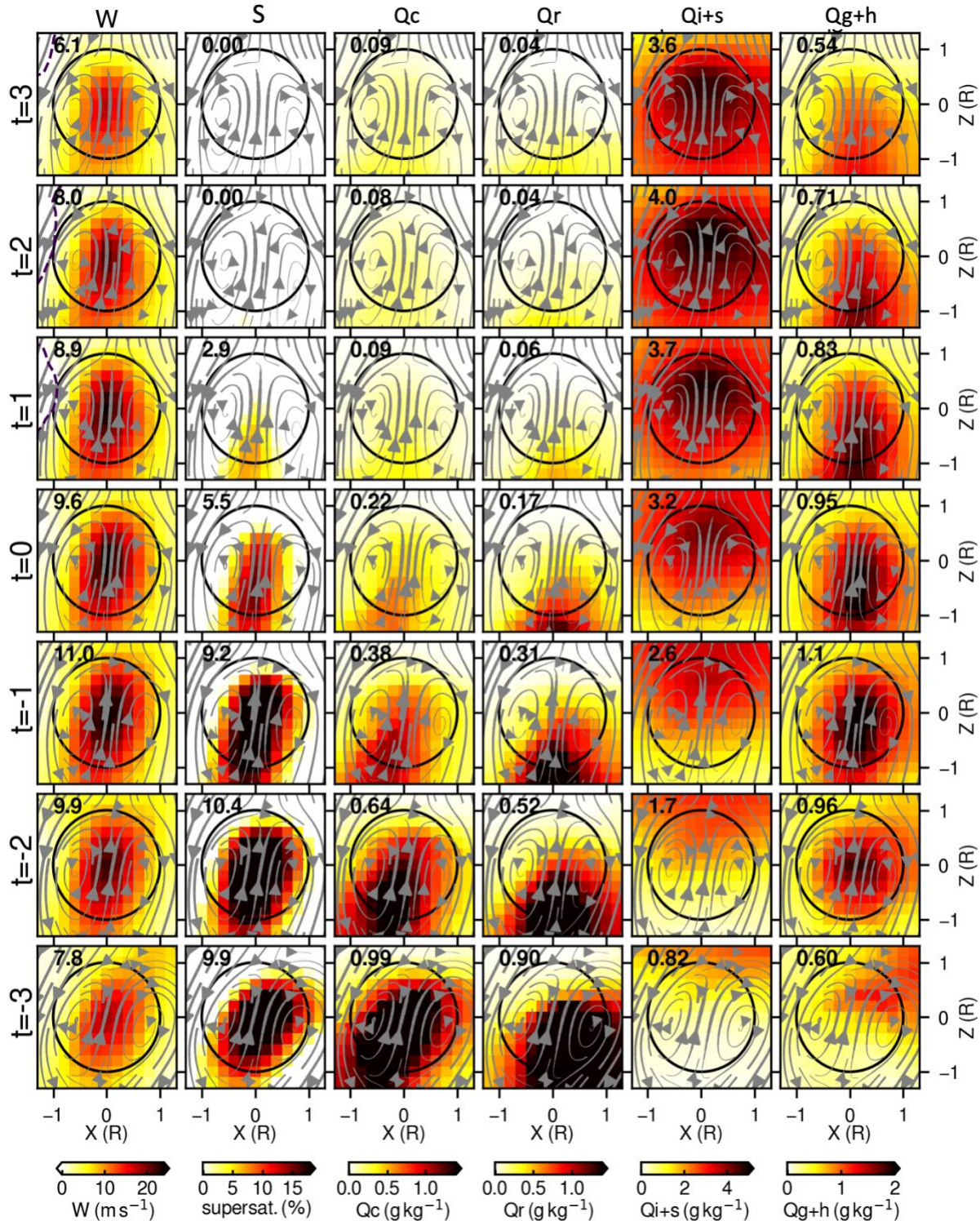
1249

Figure 10. Time series of cross sections along the x-z plane of thermal mean values of vertical velocity, supersaturation values, cloud droplet mass concentration (Qc), rain mass concentration (Qr), (e) ice and snow mass concentration (Qi+s), and graupel and hail mass concentration (Qg+h), for composites of all tracked thermals scaled by their radius. The time unit is minute.
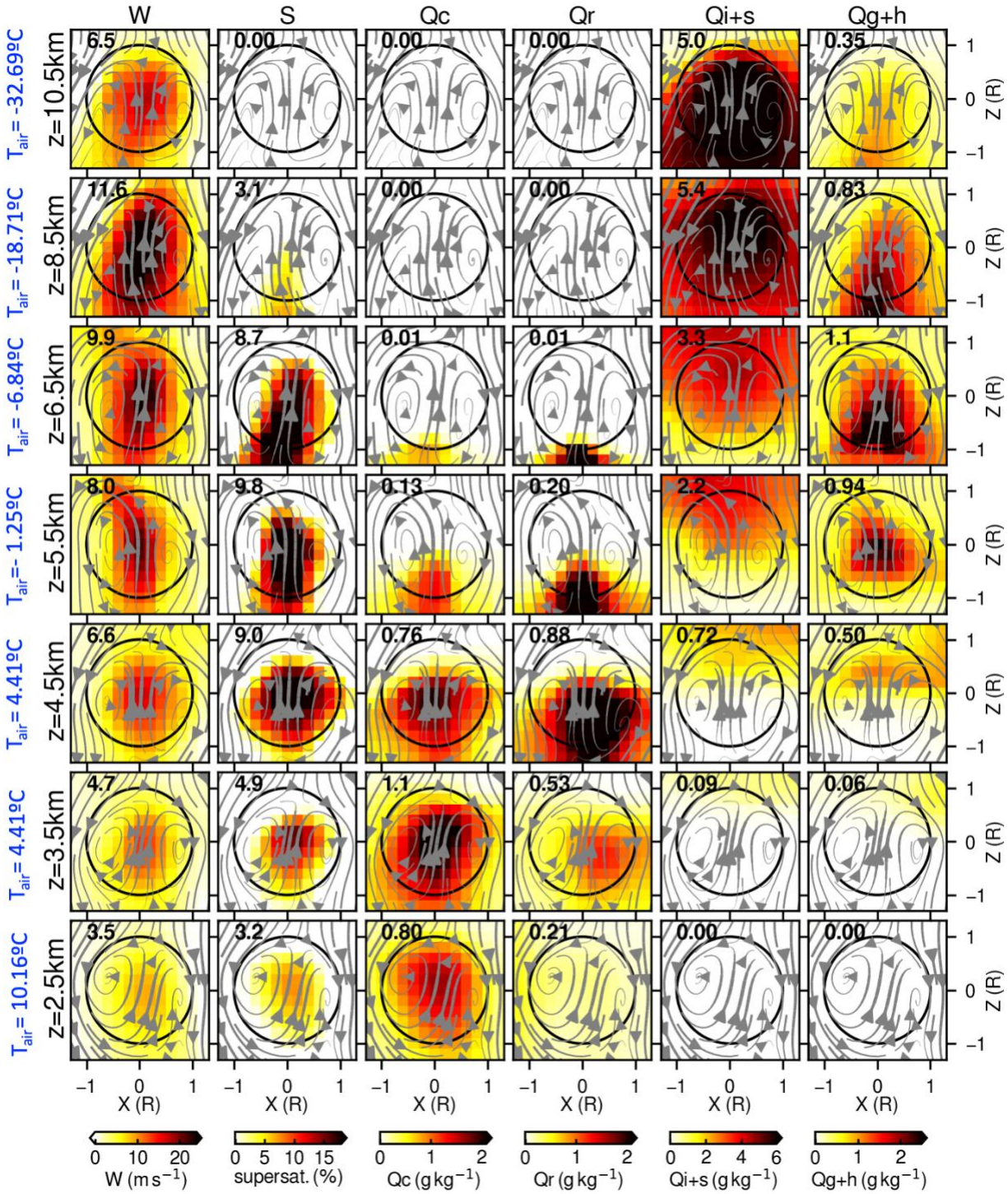
1254
1255 Figure 11. Similar to Fig. 10, but composited at different altitude levels. Note that the shade scales
1256 are different from Fig. 10 for clarity.
1257
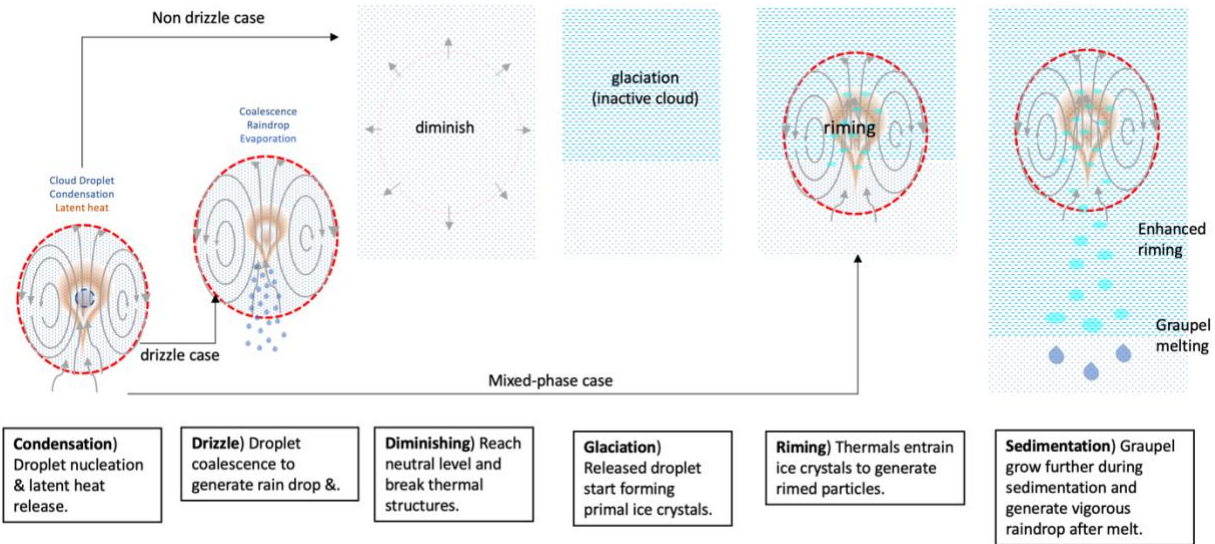
1258

1259   a)
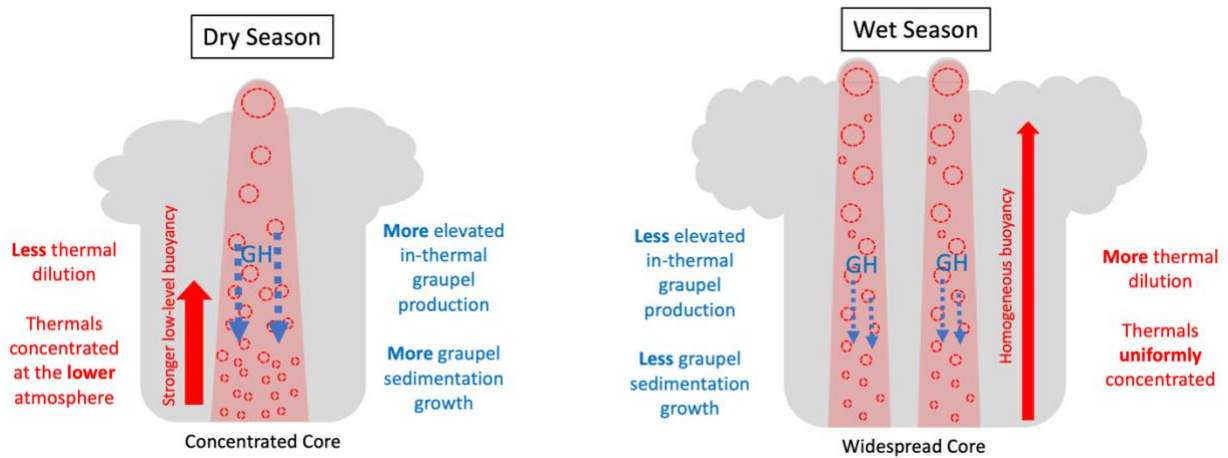
1260

1261   b)

1262   Figure 12. (a) Diagram of the suggested mechanisms for generating graupel and hail through
1263   thermal processes. (b) Diagram of thermal characteristics in deep convection in the dry and wet
1264   seasons.
1265